

2015-01-01

# Development Of Rigorous Electromagnetic Simulation Tools For Anisotropic Structures

Jose Luis Enriquez

*University of Texas at El Paso*, [jlenriquez2@miners.utep.edu](mailto:jlenriquez2@miners.utep.edu)

Follow this and additional works at: [https://digitalcommons.utep.edu/open\\_etd](https://digitalcommons.utep.edu/open_etd)



Part of the [Electrical and Electronics Commons](#), and the [Electromagnetics and Photonics Commons](#)

---

## Recommended Citation

Enriquez, Jose Luis, "Development Of Rigorous Electromagnetic Simulation Tools For Anisotropic Structures" (2015). *Open Access Theses & Dissertations*. 1036.

[https://digitalcommons.utep.edu/open\\_etd/1036](https://digitalcommons.utep.edu/open_etd/1036)

This is brought to you for free and open access by DigitalCommons@UTEP. It has been accepted for inclusion in Open Access Theses & Dissertations by an authorized administrator of DigitalCommons@UTEP. For more information, please contact [lweber@utep.edu](mailto:lweber@utep.edu).

DEVELOPMENT OF RIGOROUS ELECTROMAGNETIC SIMULATION  
TOOLS FOR ANISOTROPIC STRUCTURES

JOSE LUIS ENRIQUEZ JR.

Department of Electrical and Computer Engineering

APPROVED:

---

Raymond C. Rumpf, Ph.D., Chair

---

Deidra Hodges, Ph.D.

---

Peter Kim, Ph.D.

---

Scott Starks, Ph.D.

---

Charles Ambler, Ph.D.  
Dean of the Graduate School

Copyright ©

by

Jose Luis Enriquez Jr.

2015

## **Dedication**

This work is dedicated to my family and fellow lab mates with in the EM Lab.



DEVELOPMENT OF RIGOROUS ELECTROMAGNETIC SIMULATION  
TOOLS FOR ANISOTROPIC STRUCTURES

by

JOSE LUIS ENRIQUEZ JR., B.S.E.E.

THESIS

Presented to the Faculty of the Graduate School of  
The University of Texas at El Paso  
in Partial Fulfillment  
of the Requirements  
for the Degree of

MASTER OF SCIENCE

Department of Electrical and Computer Engineering

THE UNIVERSITY OF TEXAS AT EL PASO

May 2015

## **Acknowledgements**

Thank you, Dr. Raymond Rumpf, for your constant patience and always pushing me beyond my self-imposed limits.

Thanks to The EM Lab Members:

Recent Graduates:

Javier Pazos

Jay Barton

Current member:

Eric Berry

## **Abstract**

Many times, mankind's creative nature has pushed the envelope beyond what was deemed physically possible at the time. People have engineered ways for us to fly, communicate across the globe in seconds, landed on the moon, and more recently discovered ways to make an object invisible. Unfortunately, there are times that this creativeness is hindered by funding, access to required tools or a combination of both. While this work cannot provide funding, it does provide a tool that one could use to model and simulate a variety of media. The media can vary from devices already being implemented to more complex materials like anisotropic metamaterials. Some of these anisotropic metamaterials are currently being investigated for use in the areas of near field spectroscopy, cloaking, Dyakonov surface waves, and much more. These three topics require exotic materials with properties not found in nature, and the simulation tools currently available are quite costly to the normal consumer. This work aims to provide an algorithm to analyze complex anisotropic structures that can be implemented in any coding environment and opening the doors for more minds to play and invent new applications using these fascinating electromagnetic anisotropic materials.

## Table of Contents

Acknowledgements.....	v
Abstract.....	vi
Table of Contents.....	vii
List of Tables .....	viii
List of Figures.....	ix
Chapter 1: Introduction.....	1
Chapter 2: Theory of Dyakonov Surface Waves.....	3
2.1: Background.....	6
2.2 Dyakonov Studies .....	7
Chapter 3: Model Methodology and Development .....	12
3.1 Maxwell's Equations for AFDFD .....	12
3.2 Surface Wave Analysis.....	28
3.3 3D Anisotropic FDFD for Scattering Analysis .....	32
Chapter 4: Results.....	41
Chapter 5: Conclusion .....	55
References.....	56
Vita... ..	58

## **List of Tables**

Table 2-1 Table of Mineralogical Crystals[12] .....	7
---	---

## List of Figures

Figure 2.1 Simple DSW configuration. ....	4
Figure 2.2 Takayama experiment[2].....	6
Figure 2.3 LHM Lattice [13]. ....	8
Figure 2.4 Example of Dyakonov-Tamm Wave Configuration[2]. ....	9
Figure 2.5 Chiral sculptured thin film[2],[14]. ....	10
Figure 2.6 Artificially anisotropic substrate that supports a DSW. ....	11
Figure 3.1 Yee cell.....	17
Figure 3.2 Field placement on a high resolution grid[22] .....	23
Figure 3.3 TF/SF Sample Configuration .....	36
Figure 4.1 DSW basic configuration. ....	41
Figure 4.2 Example of surface modes. ....	42
Figure 4.3 DSW Centered of AED. ....	43
Figure 4.4 DSW Off Center of AED. ....	44
Figure 4.5 DSW Near Max of AED. ....	44
Figure 4.6 DSW transition out of AED. ....	45
Figure 4.7 Physical limitation study .....	46
Figure 4.8 Effect of cladding on center point of the AED.....	47
Figure 4.9 DSW AED Max Cut Off[7]. ....	48
Figure 4.10 Width of AED .....	49
Figure 4.11 Effect of the birefringence and cladding on the AED. ....	50
Figure 4.12 Frequency effect on the propagation constant.....	51
Figure 4.13 DSW Experimental Configuration[7]. ....	52
Figure 4.14 Torner DSW Analytical Configurations[24].....	52
Figure 4.15 DSW Torner Simulation[24].....	53
Figure 4.16 Polar Spectroscopy Verification.....	53

## Chapter 1: Introduction

Current academia has had a flux of marvelous discoveries that were once considered science-fiction and not physically achievable by our current technology. For example, researchers were able to take an item and cloak it or rather make it invisible to certain spectrums of light. They also created a way to produce images at resolutions smaller than a wavelength. Another group created a way to bend or manipulate waves using printable plastic. The previous advancements were made possible by engineering special anisotropic materials that produced special properties tailored for each end product. The actual fabrication of these special materials is not simple nor is it cheap. These capabilities took tremendous amounts of time to imagine, model and analyze before becoming a reality. Applications like HFSS and COMSOL that have algorithms to solve Maxwell's equations inside complex anisotropic materials like these, but these programs cost many thousands of dollars for a single license and in most cases the cost is actually a yearly subscription. While these packages are powerful and relatively easy to use, it would be more advantageous if something cheaper were available to enable more minds to create new possibilities with these anisotropic materials and their properties.

This work presents one such package or rather an algorithm for modeling complex anisotropic media. The results presented within were developed with MATLAB as the interface, but the methodology is presented such a way, that it can be implemented in any environment the user is most comfortable with. Unlike Ansys HFSS and COMSOL, the algorithm presented in this work solves only electromagnetic phenomena, but it allows researchers to explore the realm of complex anisotropic materials, such as uniaxial crystals, left handed materials, double negative materials, and other engineered materials. These materials are used for sub-wavelength imagery and surface wave excitation to just name a few.

Chapter 2 will introduce the topic of Dyakonov surface waves, which is an electromagnetic phenomenon of growing interest to replace the lossy surface plasmon polaritons. The topic of the Dyakonov surface wave serves as a good illustration of this algorithm's flexibility with the very complicated and arbitrarily oriented material parameters required to excite these hybrid waves. This

chapter will also give some background on the various ways these hybrid electromagnetic waves have been studied and some theories on their possible applications. There are few experimental results for this specific type of wave due to their very stringent requirements for existence. More research is needed in order to provide better means of creating and controlling these waves before we can effectively harness their unique characteristics.

Chapter 3 is a comprehensive description on how the algorithm rigorously solves Maxwell's equations for both a surface wave analysis and full 3D anisotropic steady state model. This break down is tailored for but not limited to MATLAB.

Chapter 4 covers the results of testing this model by analyzing the difficult Dyakonov surface waves, as a means to verify its capabilities of modeling complex anisotropic materials.



## Chapter 2: Theory of Dyakonov Surface Waves

In 1988 Mikhail I. Dyakonov mathematically derived the existence of a new kind of wave localized to the interface between two materials where at least one is anisotropic. There are a few material configurations that support this specific type electromagnetic wave. The two most common configurations require an isotropic cladding on top of either positive uniaxial or biaxial substrate. The wave is said to exist solely on the symmetry created at the intersecting boundary of the two materials. Which is completely unlike other types of wave phenomena like acoustic waves and surface plasmon polaritons (SPP). The required material geometry is a combination of the extraordinary ( $\epsilon_e$ ) and ordinary permittivity ( $\epsilon_o$ ) of the crystalline structure, and the isotropic superstrate with a permittivity ( $\epsilon_s$ ). The required crystalline properties for the positive uniaxial case are given by equation (1.1).

$$n_o < n_s < n_e \text{ or } n_{\perp} < n_s < n_{\parallel} \quad (1.1)$$

Here  $n_i = \sqrt{\epsilon_i}$  as formulated by Dyakonov [1]. The general existence condition required for the biaxial crystal case, as stated in [2], are

$$n_3 < n_2 < n_s < n_1 \quad (1.2)$$

given that

$$n_1 = \max(n_x, n_y, n_z) \quad (1.3)$$

and

$$n_3 = \min(n_x, n_y, n_z) \quad (1.4)$$

The scope of this research focuses on the positive uniaxial case. However, it is important to address both the uniaxial and biaxial cases and clarify that the method, described later, is capable of modeling any configuration and inhomogeneity of anisotropy.

For either case, the simplest orientation of the crystal and cladding is with the optical axis of the system contained within the plane of the interface between the two materials. For example, the optic axis of the uniaxial crystal in Figure 2.1 is contained in the dark (blue)  $x$ - $y$  plane. Surface wave propagation is allowed within this plane at some angle defined as  $\angle OA$ .

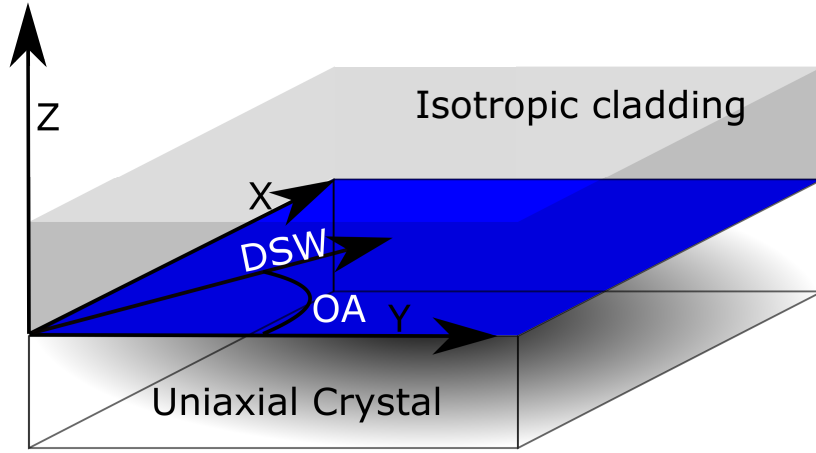


Figure 2.1 Simple DSW configuration.

Due to this required relationship at the interface, there exists a small range of angles that support a DSW. This small range of angles is known as the angular existence domain (AED). For an isotropic-uniaxial structure the angular existence domain is governed by three angles shown in equations (1.5-1.7). Ref [1] describes the minimum angle of angular existence as

$$\sin^2(\theta_{\min}) = \frac{\xi}{2} \left[ (1 - \rho\xi) + \sqrt{(1 - \rho\xi)^2 + 4\rho} \right] \quad (1.5)$$

While the max allowed angle is constrained to

$$\sin^2(\theta_{\max}) = \frac{\xi(1 + \rho)^3}{(1 + \rho)^2(1 + \rho\xi) - \rho^2(1 + \xi)^2} \quad (1.6)$$

Both equations (1.5) and (1.6) are centralized around

$$\theta_{center} \approx \sin^{-1} \left( \sqrt{\frac{\xi(\rho + 1)}{\xi\rho + 1}} \right) \quad (1.7)$$

For the case of isotropic-biaxial crystal arrangement, the allowed range of propagation is defined by equations (1.8) and (1.9) [2]. The minimum allowed angle in the case of biaxial crystal symmetry is

$$\sin(\theta_{\min}) = \sqrt{\left( \frac{v}{v_1} \right)^* \frac{1}{1 + v(v_1 - v)^2 / (1 + v_1)(v_2 - v) + v(v_1 - v)}} \quad (1.8)$$

While the maximum allowed angle is defined as

$$\sin(\theta_{\max}) = \sqrt{\frac{v}{v_1} + \frac{1}{2v_1(1+v)^2} \left[ (1+v_1)(v_2-v) + 2v(1+v)^*(v_1-v) - \sqrt{(1+v_1)(v_2-v)[(1+v_1)(v_2-v) + 4v(1+v)(v_1-v)]} \right]} \quad (1.9)$$

Given that

$$v = \frac{\epsilon_1}{\epsilon_s} - 1, \quad v_1 = \frac{\epsilon_3}{\epsilon_1} - 1, \quad v_2 = \frac{\epsilon_3}{\epsilon_2} - 1, \text{ and } \epsilon_1 > \epsilon_s > \epsilon_2 > \epsilon_3 \text{ as stated in [2].}$$

The surface waves excited under the above conditions are considered to be hybrid waves [3],[4]. They are considered hybrid because they are composed one pair of ordinary and extraordinary waves in the crystal and one pair of TE and TM waves in the isotropic slab [1]. The energy of the surface waves are not completely confined at the interface, but are optimally confined at the central angle. As the wave begins to stray away from the central angle, towards the minimum allowed angle the wave profile begins to shift into the isotropic cladding until it exits the allowed range and become a propagating mode in the cladding. Similarly, as the angle of the waves propagation begins to march towards maximum allowed angle the profile transfers to the crystal until it becomes coupled into an extraordinary wave [1], [2].

Unfortunately, there are very few naturally occurring crystals that satisfy all of the previously mentioned requirements. The few crystals that do satisfy the requirements have a very small variation between the ordinary and extraordinary parameters (birefringence) making the span of existence angles extremely small. This small birefringence has made exciting these surface waves very difficult. It was 21 years between the time they were predicted and the very first experimental excitation. We hope that by producing a means to simulate engineered material characteristics, and their experimental results, future work can be limited only by the capabilities used to manufacture these artificial materials.

## 2.1: BACKGROUND

To date, there have been numerous studies on this specific type of surface wave and the phenomena similar to them. This is due to a renewed interest fueled by the notion that Dyakonov surface waves could be used in applications such as integrated optics, optical interconnects, surface interrogation, chemical/biological sensing which would replace the currently use surface plasmon polaritons in these and other applications [5], [6]. Each of the following sections will provide a brief overview on the types of studies, from the actual excitation of true Dyakonov surface waves to DSW like phenomena, currently being done in this area of electromagnetics.

### 2.1.1 Excitation of Dyakonov Surface Waves

Very few studies however have been on actually exciting and recording Dyakonov surface waves. The first observed Dyakonov surface wave was by Dr. Osamu Takayama and a team of fellow researchers using a modified Otto-Kretchman configuration, seen in Figure 2.2, of an isotropic medium and positive uniaxial crystal. The Otto-Kretchman configuration uses a prism to help spectrally separate the surface wave from the regular Fabry-Perot modes that could be excited simultaneously in the isotropic substrate.

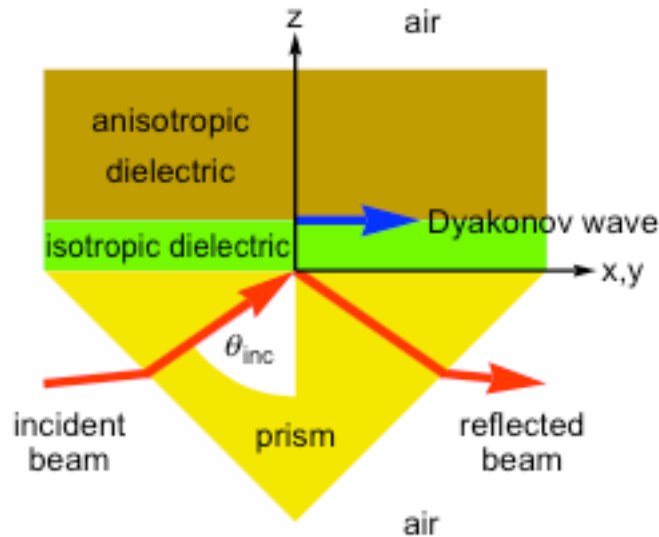


Figure 2.2 Takayama experiment[2].

By utilizing the polarization conversion that occurs when a hybrid mode is excited at the surface of an anisotropic medium, Takayama and his group were able to record, using a CCD camera, the bright reflection correlating to excitation of the elusive DSW phenomena [7].

After the first observation of the DSW, Takayama and the team of fellow researchers simulated two more configurations to further confirm the physical existence of these waves. One configuration used a similar Otto-Kretschman set up but this time the two slabs were both biaxial crystals [8]. The last configuration proved that these hybrid waves could be use to excite guided modes in thin films with their thicknesses are much smaller than the cut off thickness dictated by standard waveguides [9]. This is a promising find, as it showed the ability to harness these highly localized waves in the application of thin film wave guiding which currently uses SPPs. This find would support those who hypothesize these waves would be suitable replacements for the lossy surface plasmon polaritons currently being implemented in areas like plasmonics, sub-wavelength microscopy, near field optical sensors, surface sensing, and planar photonic devices to name a few [1], [3], [5], [6], [10].

There are several studies being done from a theoretical standpoint on the existence of DSW in other materials like left handed media, biaxial-biaxial crystalline structures and using materials with the optical axis at a tilt from the plane of the interface [11]. There has also been research done that produced a table of crystals, shown in Table 2-1, that could be used to generate DSW's by twisting the optical planes of the two materials along the axis normal to them.

Table 2-1 Table of Mineralogical Crystals[12]

Crystal	$\delta$	$n_c - n_a$	$\bar{\epsilon}$	$\xi_{max}$
Hemimorphite	21.6°	0.022	1.027	68.4°
Crocoite	23.7°	0.35	1.326	66.3°
Tellurite	44.7°	0.035	1.381	45.3°
Cerussite	84.9°	0.273	1.326	5.1°
Witherite	85.2°	0.148	1.203	4.8°

## 2.2 DYAKONOV STUDIES

Other researchers have experimented with more exotic materials like chiral, left hand materials (LHM), and linearly optic materials to enhance the existence domain of this specific type of surface

waves. However, the results of these studies are Dyakonov-like reactions, as they do not follow the requirements or have all characteristics of this type of surface wave as described by Dyakonov in 1988. Some examples of such phenomena are briefly mentioned below.

### 2.2.1 DSWs Supported by Left-Handed Materials

Among the few studies done on DSWs using left handed materials; there were a couple that used periodic metal-dielectric (MD) lattice to excite the DSWs [5], [13]. The use of this artificial material structure, supports the growing trend that engineered materials could be created to excite these elusive hybrid waves and relax the stringent conditions governing their propagation. The lattice from their simulation, based on the finite element method (FEM), is shown in Figure 2.3.

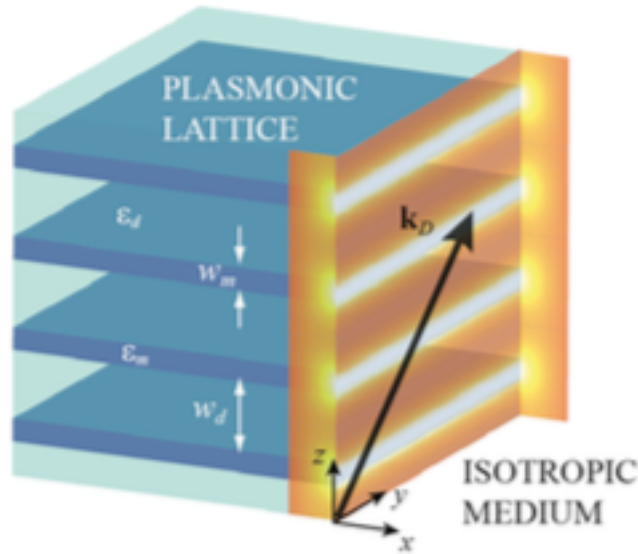


Figure 2.3 LHM Lattice [13].

Other LHM studies elucidated on the existence of Dyakonov like plasmons, referred to as Dyakonov plasmons, to explain operation of a super lens capable of sub-wavelength imaging and possible other sensing applications [5].

### 2.2.2 Dyakonov-Tamm Waves

The use of chiral media to excite surface waves created a whole new field of study based on what are now known as Dyakonov-Tamm waves. These waves are an amalgamation of two types of

surface waves and their result differs from original DSW in that, in this case, one material as both anisotropic and periodically nonhomogeneous in a direction perpendicular to the interface plane.

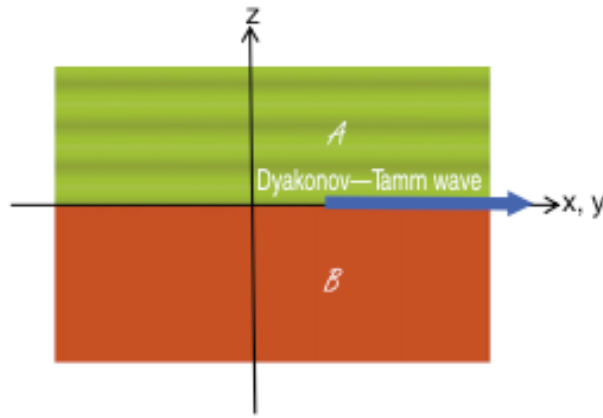


Figure 2.4 Example of Dyakonov-Tamm Wave Configuration[2].

The half-space annotated by  $A$  is an artificial engineered structured that is both periodically nonhomogeneous in a direction normal to the interface, and anisotropic. This type of material is required for the existence of Tamm waves. The anisotropy of the material could also support the DSW phenomena [2]. Under certain material conditions both surface waves can be excited simultaneously. The combination of these two distinct types of surface waves is known as a Dyakonov-Tamm wave.

A media known as chiral sculptured thin films can provide both the anisotropy and nonhomogeneity required for this type of wave. The deposition parameter marked as  $2\Omega$  in Figure 2.5 depicts the period at which the device repeats. The quantity  $X$  is the angel of inclination [14]. The combination of these two deposition parameters is what dictates the level of anisotropy and periodic nonhomogeneity the chiral film generates.

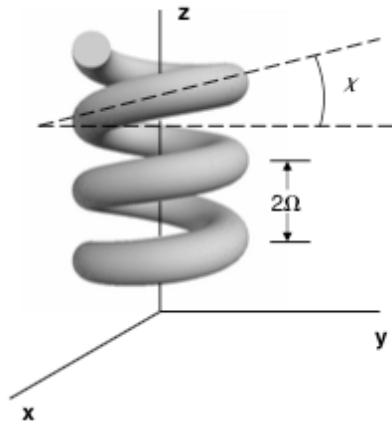


Figure 2.5 Chiral sculptured thin film[2],[14].

This particular wave has its advantages in that there is a much wider AED and it is speculated that multiple distinct surface wave modes could coexist at the interface[2].

### 2.2.3 Dyakonov Surface Waves in Linear Electro-Optic Materials

Linearly electro-optic materials require the use of an applied electric field, like the method known as the Pockels effect, to alter the material's dielectric response in order to satisfy the existence conditions stated previously. This effect changes the direction of the material's cellular arrangement which leads to an increase or decrease in certain material parameters, like dielectric strength and elasticity [15]. Utilizing this effect, the researchers were also able to arbitrarily control the direction of allowed surface wave propagation or even widen the existence domain on the surfaces of their material [15]–[17].

### 2.2.4 Photonic Crystals and Dyakonov Surface Waves

In the area of photonics, a team hypothesized that by creating a two dimensional photonic crystal, Figure 2.6, operating at the long wavelength limit, you could create the necessary positive birefringence necessary for excitation of hybrid surface waves [3].



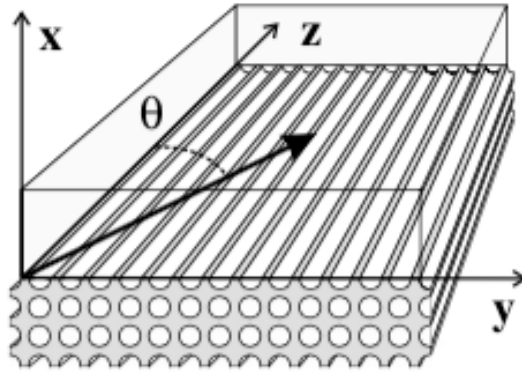


Figure 2.6 Artificially anisotropic substrate that supports a DSW.

This particular application illustrates an important point as the hypothetical photonic crystal can be engineered to meet the criteria of these hybrid waves. These artificial materials could be produced to not only excite these waves but also relax their stringent existence conditions and control their highly localized nature for suitable applications.

## Chapter 3: Model Methodology and Development

Much of the current literature available on Dyakonov surface waves is based on tedious analytical derivation of field/material interaction using the transfer matrix method (TMM) [4], [7],[9]. More specifically the TMM method was used to predict the reflectance/transmission spectra of the partnering materials, as a starting point for the physical experiments.

The proceeding finite-difference frequency-domain method was formulated to incorporate both 9-element tensors of the permittivity and permeability of any desired material in order to solve a 3D scattering problem. The formulation of the anisotropic finite-difference frequency-domain (AFDFD) is separated into three main sections. The first section encompasses the derivation of our principal equations from Maxwell's equations, to include uniaxial perfectly matched layers for a Cartesian grid. The next section takes the results of first section and manipulates them in order to model surface waves, as the modes traveling along the surface of the materials are handled or described the same as modes guided in a waveguide with a thickness approaching zero[18]. The last section is the formulation of the 3D steady-state model starting from results of section 1.

### 3.1 Maxwell's Equations for AFDFD

The method begins with the curl of the electric field, as stated in Maxwell equations, for a material that is both lossless and homogenous, one will arrive at

$$\nabla \times \vec{E} = -\frac{\partial \vec{B}}{\partial t} \quad (3.1)$$

The magnetic response equation (3.1) can be replaced with its corresponding constitutive relation, from equation (3.2)

$$\begin{aligned} \vec{D} &= [\epsilon] \vec{E} \\ \vec{B} &= [\mu] \vec{H} \end{aligned} \quad (3.2)$$

and then transformed from the time-domain to frequency-domain as

$$\nabla \times \vec{E} = -j\omega\mu_0 [\mu_r] \vec{H} \quad (3.3)$$

To reduce the possibility of error through loss of precision, i.e. computational rounding error, the magnetic field is normalized as follows.

$$\vec{\tilde{H}}(\omega) = -j\eta_0 \vec{H} \quad (3.4)$$

and rearranging terms gives us

$$\frac{\vec{\tilde{H}}}{-j\eta_0} = \vec{H} \quad (3.5)$$

This also adjusts the magnitude of the magnetic field such that it is no longer about three orders of magnitude smaller than the electric field. This alleviates confusion when comparing the field value quantities at the end of a simulation. Through the rest of the section the  $\vec{\tilde{H}}$  will denote our normalized magnetic field. The electric field could be the quantity normalized instead of the magnetic field through a similar process but this method will use the normalized magnetic field approach. Now if we substitute (3.4) back into our frequency-domain equation we have

$$\nabla \times \vec{E} = -j\omega\mu_0 [\mu_r] \frac{\vec{\tilde{H}}}{-j\eta_0} \quad (3.6)$$

Given that the free space impedance  $\eta_0 = \sqrt{\mu_0/\epsilon_0}$  along with some simple algebra

$$\nabla \times \vec{E} = \omega\sqrt{\epsilon_0\mu_0} [\mu_r] \vec{\tilde{H}} \quad (3.7)$$

This can be simplified by substituting  $k_0 = \omega\sqrt{\epsilon_0\mu_0}$ , for the wavenumber in vacuum

$$\nabla \times \vec{E} = k_0 [\mu_r] \vec{\tilde{H}} \quad (3.8)$$

Now that the normalized magnetic field has been incorporated into the curl of the electric field, the grid coordinates need to be adjusted in a similar manner. This is accomplished by scaling the grid coordinates by  $k_0$  giving

$$\begin{aligned} \tilde{x} &= k_0 x \\ \tilde{y} &= k_0 y \\ \tilde{z} &= k_0 z \end{aligned} \quad (3.9)$$

At this point it is important to address the curl of the magnetic field using the new normalized magnetic field given in eq. (3.4). The curl of the magnetic field in the time-domain is

$$\nabla \times \vec{H} = \vec{J} + \frac{\partial \vec{D}}{\partial t} \quad (3.10)$$

Converting equation (3.10) to the frequency domain while assuming no current density

$$\nabla \times \vec{H} = j\omega\epsilon_0[\epsilon_r]\vec{E} \quad (3.11)$$

Inserting the normalized magnetic field results in

$$\nabla \times \frac{\vec{H}}{-j\eta_0} = j\omega\epsilon_0[\epsilon_r]\vec{E} \quad (3.12)$$

Using the same equalities for  $k_0$  and  $\eta_0$  from above combined with some simple algebra results in

$$\nabla \times \vec{H} = k_0[\epsilon_r]\vec{E} \quad (3.13)$$

### 3.1.1 Uniaxial Perfectly Matched Layer

There are physical limitations or bounds to the simulation grid. To emulate waves traveling out of the simulation area we implement a technique known as the uniaxial perfectly matched layers (UPML)[19]. These layers absorb these outgoing waves as they travel to the bounds of modeling area. The UPML(s) are easily incorporated into Maxwell's equations represented by the matrix  $[s]$  giving

$$\begin{aligned} \nabla \times \vec{H} &= k_0[s][\epsilon_r]\vec{E} \\ \nabla \times \vec{E} &= k_0[s][\mu_r]\vec{H} \end{aligned} \quad (3.14)$$

The matrix  $[s]$  is expressed as

$$[s] = \begin{bmatrix} \frac{s_y s_z}{s_x} & 0 & 0 \\ 0 & \frac{s_x s_z}{s_y} & 0 \\ 0 & 0 & \frac{s_x s_y}{s_z} \end{bmatrix} \quad (3.15)$$

Where the terms  $s_x, s_y$  and  $s_z$  can be calculated according to[19].

$$s_x(x) = s_{x0}(x) [1 - j\eta_0 \sigma'_x(x)]$$

$$s_{x0} = 1 + s_{\max} \left( \frac{x}{L_x} \right)^p \quad (3.16)$$

$$\sigma'_x(x) = \sigma'_{\max} \sin^2 \left( \frac{\pi x}{2L_x} \right)$$

$$s_y(y) = s_{y0}(y) [1 - j\eta_0 \sigma'_y(y)]$$

$$s_{y0} = 1 + s_{\max} \left( \frac{y}{L_y} \right)^p \quad (3.17)$$

$$\sigma'_y(y) = \sigma'_{\max} \sin^2 \left( \frac{\pi y}{2L_y} \right)$$

$$s_z(z) = s_{z0}(z) [1 - j\eta_0 \sigma'_z(z)]$$

$$s_{z0} = 1 + s_{\max} \left( \frac{z}{L_z} \right)^p \quad (3.18)$$

$$\sigma'_z(z) = \sigma'_{\max} \sin^2 \left( \frac{\pi z}{2L_z} \right)$$

The term  $\sigma'$  represents a fictitious conductivity term and is annotated to avoid confusion with normal conductivity term accounted for in a complex dielectric constant. Typical vales for the above parameters are  $0 \leq s_{\max} \leq 5$ ,  $1 \leq p \leq 5$ , and  $\sigma'_{\max} = 1$ . The size of the UPML is typically between 20 and 40 cells. The variables denoted by  $L_i$  are the physical lengths of each axis associated by the dimension subscript  $i$ . These lengths are bounded in such a way that the parameters  $L_x$ ,  $L_y$ ,  $L_z$  increase from 0 to 1 across the grid [19]. For simplicity we allow the UPML terms to be absorbed into our material tensors  $[\epsilon_r]$  and  $[\mu_r]$  from here on out so that that algorithm can be formulated without considering these terms.

The expanding out the equations in (3.14) results in set of linear equations that describe each curl equation in a Cartesian coordinate system. For example, by expanding out the curl of the electric field and implementing the normalized coordinate scheme in equation (3.9), the equations in (3.14) become

$$\begin{aligned}
\frac{\partial E}{\partial \tilde{y}} - \frac{\partial E}{\partial \tilde{z}} &= \mu_{rxx} \tilde{H}_x + \mu_{rxy} \tilde{H}_y + \mu_{rxz} \tilde{H}_z \\
\frac{\partial E}{\partial \tilde{z}} - \frac{\partial E}{\partial \tilde{x}} &= \mu_{ryx} \tilde{H}_x + \mu_{ryy} \tilde{H}_y + \mu_{ryz} \tilde{H}_z \\
\frac{\partial E}{\partial \tilde{x}} - \frac{\partial E}{\partial \tilde{y}} &= \mu_{rxx} \tilde{H}_x + \mu_{rxy} \tilde{H}_y + \mu_{rxz} \tilde{H}_z
\end{aligned} \tag{3.19}$$

Doing the same for the curl of the magnetic field we have

$$\begin{aligned}
\frac{\partial \tilde{H}}{\partial \tilde{y}} - \frac{\partial \tilde{H}}{\partial \tilde{z}} &= \epsilon_{rxx} E_x + \epsilon_{rxy} E_y + \epsilon_{rxz} E_z \\
\frac{\partial \tilde{H}}{\partial \tilde{z}} - \frac{\partial \tilde{H}}{\partial \tilde{x}} &= \epsilon_{ryx} E_x + \epsilon_{ryy} E_y + \epsilon_{ryz} E_z \\
\frac{\partial \tilde{H}}{\partial \tilde{x}} - \frac{\partial \tilde{H}}{\partial \tilde{y}} &= \epsilon_{rxx} E_x + \epsilon_{rxy} E_y + \epsilon_{rxz} E_z
\end{aligned} \tag{3.20}$$

The set of six equations in (3.19) and (3.20) will describe the electric and magnetic fields throughout the grid.

The grid itself is used here is based on the Yee cell scheme. This specific scheme allows us to approximate the derivatives in Maxwell's equations with central finite differences by placing the field components on this staggered grid structure [20]. However, this does cause a problem with the center finite difference approach as the field components are not collocated but a fix for this will be addressed shortly. An example cell of a Yee structured grid is can be seen Figure 3.1 in the below.

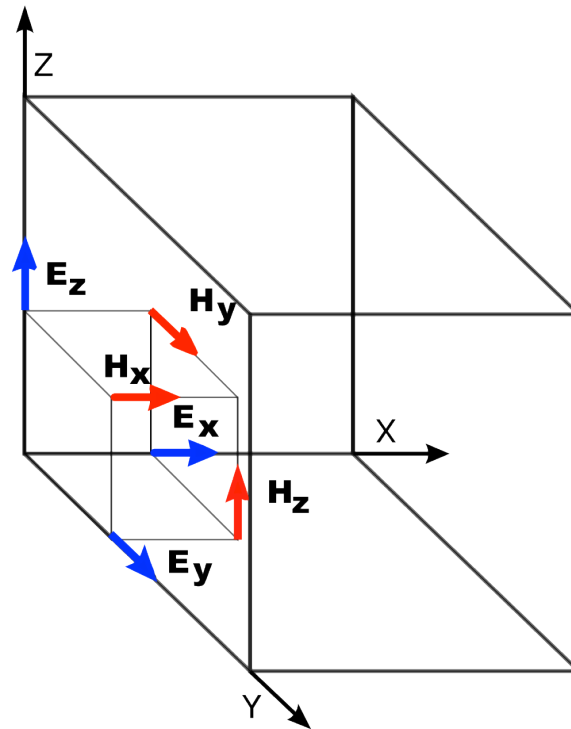


Figure 3.1 Yee cell

With the Yee cell implementation you have a grid that is divergence free, simplified mathematical calculations of curl operators and the physical boundary conditions are inherently satisfied. As mentioned previously this grid layout causes a problem with the finite-difference approach because the finite difference equation assumes that its terms are located at the same physical locations in space. In the Yee cell the terms are not collocated, so equations (3.19) and (3.20) must be interpolated to a common point. The expanded equations that follow are the results of implementing interpolation into these sets of equations. The interpolation is done using the four points that surround the current position being evaluated. This places the current position as the center position in relation to the four surrounding points thus satisfying the central finite difference equation. Starting with the curl of the electric field equations, we expand out the terms to show their grid locations and the fixes associated with the problematic terms.

$$\begin{aligned}
\frac{E_z^{i,j+1,k} - E_z^{i,j,k}}{\Delta \tilde{y}} - \frac{E_y^{i,j,k+1} - E_y^{i,j,k}}{\Delta \tilde{z}} &= \mu_{rxx}^{i,j,k} \tilde{H}_x + \\
&\frac{\mu_{rxy}^{i,j,k} \tilde{H}_y^{i,j,k} + \mu_{rxy}^{i-1,j,k} \tilde{H}_y^{i-1,j,k} + \mu_{rxy}^{i,j+1,k} \tilde{H}_y^{i,j+1,k} + \mu_{rxy}^{i-1,j+1,k} \tilde{H}_y^{i-1,j+1,k}}{4} + \\
&\frac{\mu_{rxz}^{i,j,k} \tilde{H}_z^{i,j,k} + \mu_{rxz}^{i,j,k+1} \tilde{H}_z^{i,j,k+1} + \mu_{rxz}^{i-1,j,k+1} \tilde{H}_z^{i-1,j,k+1} + \mu_{rxz}^{i-1,j,k} \tilde{H}_z^{i-1,j,k}}{4}
\end{aligned} \quad (3.21)$$

$$\begin{aligned}
\frac{E_x^{i,j+1,k} - E_x^{i,j,k}}{\Delta \tilde{z}} - \frac{E_z^{i,j+1,k} - E_z^{i,j,k}}{\Delta \tilde{x}} &= \\
&\frac{\mu_{ryx}^{i,j,k} \tilde{H}_x^{i,j,k} + \mu_{ryx}^{i+1,j,k} \tilde{H}_x^{i+1,j,k} + \mu_{ryx}^{i,j-1,k} \tilde{H}_x^{i,j-1,k} + \mu_{ryx}^{i+1,j-1,k} \tilde{H}_x^{i+1,j-1,k}}{4} + \\
&\mu_{ryy}^{i,j,k} \tilde{H}_y^{i,j,k} + \\
&\frac{\mu_{ryz}^{i,j,k} \tilde{H}_z^{i,j,k} + \mu_{ryz}^{i,j,k+1} \tilde{H}_z^{i,j,k+1} + \mu_{ryz}^{i,j-1,k+1} \tilde{H}_z^{i,j-1,k+1} + \mu_{ryz}^{i,j-1,k} \tilde{H}_z^{i,j-1,k}}{4}
\end{aligned} \quad (3.22)$$

$$\begin{aligned}
\frac{E_y^{i,j+1,k} - E_y^{i,j,k}}{\Delta \tilde{x}} - \frac{E_x^{i,j+1,k} - E_x^{i,j,k}}{\Delta \tilde{y}} &= \\
&\frac{\mu_{rxx}^{i,j,k} \tilde{H}_x^{i,j,k} + \mu_{rxx}^{i+1,j,k} \tilde{H}_x^{i+1,j,k} + \mu_{rxx}^{i+1,j,k-1} \tilde{H}_x^{i+1,j,k-1} + \mu_{rxx}^{i,j,k-1} \tilde{H}_x^{i,j,k-1}}{4} + \\
&\frac{\mu_{rxy}^{i,j,k} \tilde{H}_y^{i,j,k} + \mu_{rxy}^{i,j+1,k} \tilde{H}_y^{i,j+1,k} + \mu_{rxy}^{i,j+1,k-1} \tilde{H}_y^{i,j+1,k-1} + \mu_{rxy}^{i,j,k-1} \tilde{H}_y^{i,j,k-1}}{4} + \\
&\mu_{rzz}^{i,j,k} \tilde{H}_z^{i,j,k}
\end{aligned} \quad (3.23)$$

The interpolation corrections for the curl of the magnetic field are

$$\begin{aligned}
\frac{\tilde{H}_z^{i,j,k} - \tilde{H}_z^{i,j,k-1}}{\Delta \tilde{y}} - \frac{\tilde{H}_y^{i,j,k} - \tilde{H}_y^{i,j,k-1}}{\Delta \tilde{z}} &= \varepsilon_{rxx}^{i,j,k} E_x + \\
&\frac{\varepsilon_{rxy}^{i,j,k} E_y^{i,j,k} + \varepsilon_{rxy}^{i,j-1,k} E_y^{i,j-1,k} + \varepsilon_{rxy}^{i+1,j-1,k} E_y^{i+1,j-1,k} + \varepsilon_{rxy}^{i+1,j,k} E_y^{i+1,j,k}}{4} + \\
&\frac{\varepsilon_{rxz}^{i,j,k} E_z^{i,j,k} + \varepsilon_{rxz}^{i,j,k-1} E_z^{i,j,k-1} + \varepsilon_{rxz}^{i+1,j,k-1} E_z^{i+1,j,k-1} + \varepsilon_{rxz}^{i+1,j,k} E_z^{i+1,j,k}}{4}
\end{aligned} \quad (3.24)$$

$$\begin{aligned}
\frac{\tilde{H}_x^{i,j,k} - \tilde{H}_x^{i,j,k-1}}{\Delta \tilde{z}} - \frac{\tilde{H}_z^{i,j,k} - \tilde{H}_z^{i-1,j,k}}{\Delta \tilde{x}} &= \\
&\frac{\varepsilon_{ryx}^{i,j,k} E_x^{i,j,k} + \varepsilon_{ryx}^{i,j+1,k} E_x^{i,j+1,k} + \varepsilon_{ryx}^{i-1,j+1,k} E_x^{i-1,j+1,k} + \varepsilon_{ryx}^{i-1,j,k} E_x^{i-1,j,k}}{4} + \\
&\varepsilon_{ryy}^{i,j,k} E_y^{i,j,k} + \\
&\frac{\varepsilon_{ryz}^{i,j,k} E_z^{i,j,k} + \varepsilon_{ryz}^{i,j,k-1} E_z^{i,j,k-1} + \varepsilon_{ryz}^{i,j+1,k-1} E_z^{i,j+1,k-1} + \varepsilon_{ryz}^{i,j+1,k} E_z^{i,j+1,k}}{4}
\end{aligned} \quad (3.25)$$



$$\begin{aligned}
& \frac{\tilde{H}_y^{i,j,k} - \tilde{H}_y^{i,j,k-1}}{\Delta \tilde{x}} - \frac{\tilde{H}_x^{i,j,k} - \tilde{H}_x^{i,j-1,k}}{\Delta \tilde{y}} = \\
& \frac{\epsilon_{rx}^{i,j,k} E_x^{i,j,k} + \epsilon_{rx}^{i-1,j,k} E_x^{i-1,j,k} + \epsilon_{rx}^{i,j,k+1} E_x^{i,j,k+1} + \epsilon_{rx}^{i,j,k+1} E_x^{i,j,k+1}}{4} + \\
& \frac{\epsilon_{ry}^{i,j,k} E_y^{i,j,k} + \epsilon_{ry}^{i,j-1,k} E_y^{i,j-1,k} + \epsilon_{ry}^{i,j-1,k+1} E_y^{i,j-1,k+1} + \epsilon_{ry}^{i,j,k+1} E_y^{i,j,k+1}}{4} + \\
& \epsilon_{rz}^{i,j,k} E_z^{i,j,k}
\end{aligned} \tag{3.26}$$

What we have done is shown where the interpolated terms are located on the grid in relation to the terms being evaluated using their associated grid indices. For example, in equation(3.21) the off diagonal terms, the two to the right of  $E_x$ , must be interpolated or averaged around the point in space at which  $E_x$  exists. This same process is applied to every equation form (3.21) to (3.26). The interpolation matrices are

$$R_{i,j,k}^+ = \frac{R_{i+1,j,k} + R_{i,j,k}}{2} \tag{3.27}$$

$$R_{i,j,k}^+ = \frac{R_{i,j+1,k} + R_{i,j,k}}{2} \tag{3.28}$$

$$R_{i,j,k}^+ = \frac{R_{i,j,k+1} + R_{i,j,k}}{2} \tag{3.29}$$

as described in [21]. However this only interpolates from one direction at a time. The full fix requires interpolation from any direction due to the staggering of the field components on the grid. The matrix operator is  $R_i^+$  interpolates from the next cell over in the positive  $i^{th}$  dimension. A different matrix operator  $R_i^-$  interpolates from the previous cell in the  $i^{th}$  dimension. The two matrices are related through the Hermitian operation  $\mathbf{R}_i^+ = (\mathbf{R}_i^-)^H$ .

Each of the equations in (3.21)-(3.26) are applied to each point throughout the grid. This results in a large set of numerical equations. These sets of equations can be written as matrices, which result in

$$\begin{aligned}
\mathbf{D}_{\tilde{y}z}^h \tilde{\mathbf{h}} - \mathbf{D}_{\tilde{z}y}^h \tilde{\mathbf{h}} &= \epsilon_{rx} \mathbf{e}_x + \epsilon_{rx} \mathbf{R}_x^+ \mathbf{R}_y^- \mathbf{e}_y + \epsilon_{rx} \mathbf{R}_x^+ \mathbf{R}_z^- \mathbf{e}_z \\
\mathbf{D}_{\tilde{z}x}^h \tilde{\mathbf{h}} - \mathbf{D}_{\tilde{x}z}^h \tilde{\mathbf{h}} &= \epsilon_{ry} \mathbf{R}_x^- \mathbf{R}_y^+ \mathbf{e}_x + \epsilon_{ry} \mathbf{e}_y + \epsilon_{ry} \mathbf{R}_y^+ \mathbf{R}_z^- \mathbf{e}_z \\
\mathbf{D}_{\tilde{x}y}^h \tilde{\mathbf{h}} - \mathbf{D}_{\tilde{y}x}^h \tilde{\mathbf{h}} &= \epsilon_{rz} \mathbf{R}_x^- \mathbf{R}_z^+ \mathbf{e}_x + \epsilon_{rz} \mathbf{R}_y^+ \mathbf{R}_z^+ \mathbf{e}_y + \epsilon_{rz} \mathbf{e}_z
\end{aligned} \tag{3.30}$$

$$\begin{aligned}
\mathbf{D}_{\tilde{y}z}^e \mathbf{e}_z - \mathbf{D}_{\tilde{z}y}^e \mathbf{e}_y &= \mu_{rxx} \tilde{\mathbf{h}}_x + \mu_{rxy} \mathbf{R}_x^- \mathbf{R}_y^+ \tilde{\mathbf{h}}_y + \mu_{rxz} \mathbf{R}_x^- \mathbf{R}_z^+ \tilde{\mathbf{h}}_z \\
\mathbf{D}_{\tilde{z}x}^e \mathbf{e}_x - \mathbf{D}_{\tilde{x}z}^e \mathbf{e}_z &= \mu_{ryx} \mathbf{R}_x^+ \mathbf{R}_y^- \tilde{\mathbf{h}}_x + \mu_{ryy} \tilde{\mathbf{h}}_y + \mu_{ryz} \mathbf{R}_y^- \mathbf{R}_z^+ \tilde{\mathbf{h}}_z \\
\mathbf{D}_{\tilde{x}y}^e \mathbf{e}_y - \mathbf{D}_{\tilde{y}x}^e \mathbf{e}_x &= \mu_{rzx} \mathbf{R}_x^+ \mathbf{R}_z^- \tilde{\mathbf{h}}_x + \mu_{rzy} \mathbf{R}_y^+ \mathbf{R}_z^- \tilde{\mathbf{h}}_y + \mu_{rzz} \tilde{\mathbf{h}}_z
\end{aligned} \tag{3.31}$$

The terms  $\mathbf{e}_x$ ,  $\mathbf{e}_y$ ,  $\mathbf{e}_z$ ,  $\tilde{\mathbf{h}}_x$ ,  $\tilde{\mathbf{h}}_y$  and  $\tilde{\mathbf{h}}_z$  are column vectors containing all the field components throughout the grid reshaped into linear arrays. The terms  $\boldsymbol{\epsilon}_{nm}$  and  $\boldsymbol{\mu}_{nm}$  diagonal matrices that describe material tensor elements, including the absorbed UPML terms, on the grid. The terms  $\mathbf{D}_{x,y,z}^{e,h}$  are matrices that calculate the first order derivative of electric and magnetic field components along the grid. The equations previously mention are simplified by combining the interpolation terms into the tensor elements, resulting in the equations sets (3.32) and (3.33). Here the prime indicates that the matrices of the effective material parameters have absorbed the interpolation terms.

$$\begin{aligned}
\mathbf{D}_{\tilde{y}z}^h \mathbf{h}_z - \mathbf{D}_{\tilde{z}y}^h \mathbf{h}_y &= \boldsymbol{\epsilon}'_{rxx} \mathbf{e}_x + \boldsymbol{\epsilon}'_{rxy} \mathbf{e}_y + \boldsymbol{\epsilon}'_{rxz} \mathbf{e}_z \\
\mathbf{D}_{\tilde{z}x}^h \mathbf{h}_x - \mathbf{D}_{\tilde{x}z}^h \mathbf{h}_z &= \boldsymbol{\epsilon}'_{ryx} \mathbf{e}_x + \boldsymbol{\epsilon}'_{ryy} \mathbf{e}_y + \boldsymbol{\epsilon}'_{ryz} \mathbf{e}_z \\
\mathbf{D}_{\tilde{x}y}^h \mathbf{h}_y - \mathbf{D}_{\tilde{y}x}^h \mathbf{h}_x &= \boldsymbol{\epsilon}'_{rzx} \mathbf{e}_x + \boldsymbol{\epsilon}'_{rzy} \mathbf{e}_y + \boldsymbol{\epsilon}'_{rzz} \mathbf{e}_z
\end{aligned} \tag{3.32}$$

$$\begin{aligned}
\mathbf{D}_{\tilde{y}z}^e \mathbf{e}_z - \mathbf{D}_{\tilde{z}y}^e \mathbf{e}_y &= \boldsymbol{\mu}'_{rxx} \mathbf{b}_x + \boldsymbol{\mu}'_{rxy} \mathbf{b}_y + \boldsymbol{\mu}'_{rxz} \mathbf{b}_z \\
\mathbf{D}_{\tilde{z}x}^e \mathbf{e}_x - \mathbf{D}_{\tilde{x}z}^e \mathbf{e}_z &= \boldsymbol{\mu}'_{ryx} \mathbf{b}_x + \boldsymbol{\mu}'_{ryy} \mathbf{b}_y + \boldsymbol{\mu}'_{ryz} \mathbf{b}_z \\
\mathbf{D}_{\tilde{x}y}^e \mathbf{e}_y - \mathbf{D}_{\tilde{y}x}^e \mathbf{e}_x &= \boldsymbol{\mu}'_{rzx} \mathbf{b}_x + \boldsymbol{\mu}'_{rzy} \mathbf{b}_y + \boldsymbol{\mu}'_{rzz} \mathbf{b}_z
\end{aligned} \tag{3.33}$$

At this point the algorithm will stem off in two separate methods. The first method is for anisotropic surface wave mode analysis. The second is a full 3D anisotropic FDFD method for simulating a device. The surface wave analysis solves the wave equation, as an Eigen value problem while the AFDFD a scattering model. We begin with surface wave analysis because this is how we verify that our material properties support surface wave excitation. Before using the surface wave analysis the topic of placing the material properties onto the grid properly must be addressed.

### 3.1.2 Device Construction

This section will cover how to place the device parameters; similar to the ones used below, will be placed onto grid in MATLAB. There are a few basics steps to this. The first is to define the scale and constants to be used to construct the desired model. Constants like wavelength, speed of light and dimension units like meters or millimeters. From here you define the material constants like

permeability and permittivity constants to spread across the grid. The dimensions of the device to be constructed are placed here and any other parameters like size of buffer regions (Bufs) the number of cells in the absorbing boundary conditions (NPML). In the simulations below the device dimensions are all scaled by wavelength.

The next step is to determine the appropriate number of cells to properly resolve the field interactions. A parameter called NRES is used to determine the optimal required cell quantity and size. This initial resolution is then recalculated in order to resolve the smallest device and wavelength parameters. The smallest wavelength is resolved by using a minimum cell size of

$$\Delta_{\lambda} = \frac{\min(\lambda) \div \max(\sqrt{\epsilon\mu})}{NRES} \quad (3.34)$$

The minimum device resolution required is then calculated using the smallest device dimension divided by the number of cells along that axis.

$$\Delta_d \leq d_{\min} / N_d \quad (3.35)$$

The initial grid resolution is then  $\Delta_{\min} = \min([\Delta_{\lambda}, \Delta_d])$ . The grid can be further optimized by adjusting the cell size to the critical dimension of the device, which is typically along the  $x$ , horizontal axis and  $z$ , the vertical axis, in the models below. These critical dimensions are then divided by the minimum resolution, which results in the number of cells required along that axis precisely.

$$N_x = \text{ceil}\left(\frac{d_c / d_x}{2}\right) + 1 \quad (3.36)$$

$$N_y = \text{ceil}\left(\frac{d_c / d_x}{2}\right) \quad (3.37)$$

$$N_z = \text{ceil}\left(\frac{d_c / d_z}{2}\right) \quad (3.38)$$

The longitudinal axis is always and odd number that way when the diffraction orders, used to measure power flow, are calculated, they are evenly distributed along the grid. The next step is to adjust the grid resolution one last time by

$$\Delta_i = d_i / M_i \quad (3.39)$$

The subscript  $i$  corresponds to which Cartesian axis is being evaluated and  $M$  is the number of cells previously calculated for that axis. From here you can calculate the total grid size,  $S_i$ , used for the model.

$$S_x = l_x \quad (3.40)$$

$$S_y = l_y \quad (3.41)$$

$$S_z = l_z + \text{sum}(\text{Bufs}) \quad (3.42)$$

The vertical axis, here it's the  $z$ -axis, is adjusted one more time to account for the additional regions that described the perfectly matched layer and the buffer regions. This is accomplished by

$$N_z = \text{round}(S_z/d_z) + \text{sum}(\text{NPML}) \quad (3.43)$$

followed by

$$S_z = N_z * d_z \quad (3.44)$$

At this point the grid is fully optimized but if the material properties where to be placed on this grid there could material parameters that are erroneous left out when the geometry of the device is implemented. This is because of the Yee grid scheme and components being at physically different locations with in each cell. So when you build a device directly on this grid there is a chance that the geometry only partially covers a cell resulting some field components being affected while others may not be. Figure 3.2 shows how with a circular device some cells are partially filled, affecting some field parameters and excluding others.

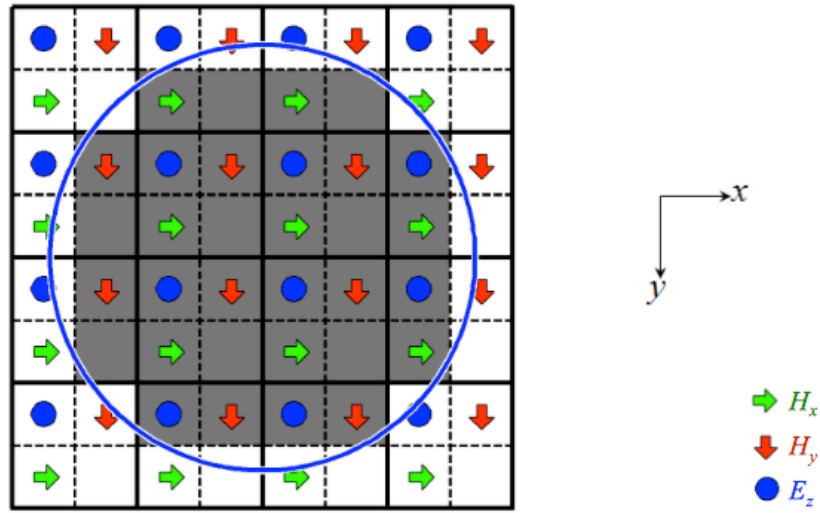


Figure 3.2 Field placement on a high resolution grid[22]

To account for this we simply double the resolution of the grid [22], while keeping the size of the grid the same, to place material parameters. Once that is accomplished then separate it back to the initial grid parameters. This means that the number of grid cells is doubled

$$N_{2x} = 2N_x \quad (3.45)$$

$$N_{2y} = 2N_y \quad (3.46)$$

$$N_{2z} = 2N_z \quad (3.47)$$

The resolution is then cut in half

$$d_{2x} = d_x / 2 \quad (3.48)$$

$$d_{2y} = d_y / 2 \quad (3.49)$$

$$d_{2z} = d_z / 2 \quad (3.50)$$

Now the grid arrays corresponding to the diagonal tensor terms,  $ER_{xx}$ ,  $ER_{yy}$  and  $ER_{zz}$ , are initialized to free space. The off diagonal terms are set to zero.

$$ER_{xx} = \text{ones}(N_{2x}, N_{2y}, N_{2z}) \quad (3.51)$$

$$ER_{xy} = \text{zeros}(N_{2x}, N_{2y}, N_{2z}) \quad (3.52)$$

$$ER_{xz} = \text{zeros}(N_{2x}, N_{2y}, N_{2z}) \quad (3.53)$$

$$ERyx = \text{zeros}(N_{2x}, N_{2y}, N_{2z}) \quad (3.54)$$

$$ERyy = \text{ones}(N_{2x}, N_{2y}, N_{2z}) \quad (3.55)$$

$$ERyz = \text{zeros}(N_{2x}, N_{2y}, N_{2z}) \quad (3.56)$$

$$ERzx = \text{zeros}(N_{2x}, N_{2y}, N_{2z}) \quad (3.57)$$

$$ERzy = \text{zeros}(N_{2x}, N_{2y}, N_{2z}) \quad (3.58)$$

$$ERzz = \text{ones}(N_{2x}, N_{2y}, N_{2z}) \quad (3.59)$$

This same procedure is repeated but for the magnetic field quantity

$$URxx = \text{ones}(N_{2x}, N_{2y}, N_{2z}) \quad (3.60)$$

$$URxy = \text{zeros}(N_{2x}, N_{2y}, N_{2z}) \quad (3.61)$$

$$URxz = \text{zeros}(N_{2x}, N_{2y}, N_{2z}) \quad (3.62)$$

$$URyx = \text{zeros}(N_{2x}, N_{2y}, N_{2z}) \quad (3.63)$$

$$URyy = \text{ones}(N_{2x}, N_{2y}, N_{2z}) \quad (3.64)$$

$$URyz = \text{zeros}(N_{2x}, N_{2y}, N_{2z}) \quad (3.65)$$

$$URzx = \text{zeros}(N_{2x}, N_{2y}, N_{2z}) \quad (3.66)$$

$$URzy = \text{zeros}(N_{2x}, N_{2y}, N_{2z}) \quad (3.67)$$

$$URzz = \text{ones}(N_{2x}, N_{2y}, N_{2z}) \quad (3.68)$$

The grid is set to receive the material properties. To build the geometry for the surface wave analysis we choose the height of the slabs to be  $h = 10 * \lambda$ . For simplicity the slabs are centered on the grid at the point  $nz = \text{round}(0.5 * N_z) - 1$ . To describe the height of the one slab it must be converted into a size in number of cells. Dividing the height by the grid resolution

$$nzh = nz - (h/d_{zz}) \quad (3.69)$$

results in this position on the grid describing the top of the slab. The height of the upper position is subtracted from the middle of the grid to account for how MATLAB indexes its arrays. These arrays

increase in size from left to right and from top to bottom. So the largest vertical index is at the lower right corner of the grid.

The upper and lower bounds of the isotropic slab are given by  $nz$  and  $nzh$ . Since the upper portion of the grid is isotropic, only the main diagonal terms arrays need to be filled. This is because an isotropic material can be represented by a tensor of form

$$[\epsilon] = \begin{bmatrix} \epsilon & 0 & 0 \\ 0 & \epsilon & 0 \\ 0 & 0 & \epsilon \end{bmatrix} \quad (3.70)$$

The elements in the diagonal material arrays between the bounds  $nz$  and  $nzh$  are set equal to the isotropic permittivity of the hypothetical DSW device, which was  $\epsilon = 1.35$ .

$$ER_{xx}(:, :, nzh : nz) = \epsilon \quad (3.71)$$

$$ER_{yy}(:, :, nzh : nz) = \epsilon \quad (3.72)$$

$$ER_{zz}(:, :, nzh : nz) = \epsilon \quad (3.73)$$

The lower anisotropic crystal is a bit more complicated as there are off tensor elements to consider. Normally an anisotropic tensor has the form

$$[\epsilon_c] = \begin{bmatrix} \epsilon_o & 0 & 0 \\ 0 & \epsilon_o & 0 \\ 0 & 0 & \epsilon_e \end{bmatrix} \quad (3.74)$$

However, in order to explore the AED of the DSW, the device needs to be rotated. This would be very hard to draw. Instead, the device rotation can be handled by rotating the material about the axis normal to the interface. This rotation can be accomplished using the rotational matrices found in Ref [25] by the angle  $\phi$ . They are

$$R_x = \begin{bmatrix} 1 & 0 & 0 \\ 0 & \cos \phi & -\sin \phi \\ 0 & \sin \phi & \cos \phi \end{bmatrix} \quad (3.75)$$

$$R_y = \begin{bmatrix} \cos\phi & 0 & \sin\phi \\ 0 & 1 & 0 \\ -\sin\phi & 0 & \cos\phi \end{bmatrix} \quad (3.76)$$

$$R_z = \begin{bmatrix} \cos\phi & -\sin\phi & 0 \\ \sin\phi & \cos\phi & 0 \\ 0 & 0 & 1 \end{bmatrix} \quad (3.77)$$

These matrices can perform multiple rotation simultaneously or one at a time. Here only one rotation is needed and is in the direction normal to the interface or the  $z$ -axis.

$$[\varepsilon_c] = [R_z][\varepsilon_c][R_z]^{-1} \quad (3.78)$$

If the result of the rotation was to at the center of the AED, the value for phi is 34 degrees and would result in a tensor below.

$$[\varepsilon_c] = \begin{bmatrix} 1.6577 & 0 & 0.8379 \\ 0 & 1.0925 & 0 \\ 0.8379 & 0 & 2.3348 \end{bmatrix} \quad (3.79)$$

If the result of the rotation was to at the center of the AED, the value for phi is 34 degrees and would result in a tensor below. The bounding points for the lower region are similar to the top except now the height of the slab is added to the mid point

$$nzl = nz + \text{round}(h/d_{2z}) \quad (3.80)$$

This sets the bounds for each material array. This time every material array will be filled with the corresponding tensor element in  $[\varepsilon_c]$ . The first subscript tells the row element and the second index indicates the column element.

$$ER_{xx}(:, :, nz+1 : nzl) = \varepsilon_{1,1} \quad (3.81)$$

$$ER_{xy}(:, :, nz+1 : nzl) = \varepsilon_{1,2} \quad (3.82)$$

$$ER_{xz}(:, :, nzh+1 : nzl) = \varepsilon_{1,3} \quad (3.83)$$

$$ER_{yx}(:, :, nz+1 : nzl) = \varepsilon_{2,1} \quad (3.84)$$

$$ER_{yy}(:, :, nz+1 : nzl) = \varepsilon_{2,2} \quad (3.85)$$



$$ER_{yz}(:, :, nzh + 1 : nzl) = \epsilon_{2,3} \quad (3.86)$$

$$ER_{zx}(:, :, nz + 1 : nzl) = \epsilon_{3,1} \quad (3.87)$$

$$ER_{zy}(:, :, nz + 1 : nzl) = \epsilon_{3,2} \quad (3.88)$$

$$ER_{zz}(:, :, nzh + 1 : nzl) = \epsilon_{3,3} \quad (3.89)$$

Now that the material parameters have been placed on the higher resolution grid, the last step is to parse this grid back to the original grid resolution. The combination of field elements staggered on the Yee grid with the higher resolution grid provides a simple solution to accomplish this as each cell contains one grid component now. Figure 3.2 actually dictates how each field element is isolated. The first two field terms,  $E_x$  and  $H_y$ , alternate vertical grid indices along the first row and continue this pattern for every other row. The last field term index begins with the second row of, first column and repeats for every other column. The alternating grid indexing can be implemented in MATLAB as

$$ER_{xx} = ER_{xx}(2:2:N_{2x}, 1:2:N_{2y}, 1:2:N_{2z}) \quad (3.90)$$

$$ER_{xy} = ER_{xy}(1:2:N_{2x}, 2:2:N_{2y}, 1:2:N_{2z}) \quad (3.91)$$

$$ER_{xz} = ER_{xz}(1:2:N_{2x}, 1:2:N_{2y}, 2:2:N_{2z}) \quad (3.92)$$

$$ER_{yx} = ER_{yx}(2:2:N_{2x}, 1:2:N_{2y}, 1:2:N_{2z}) \quad (3.93)$$

$$ER_{yy} = ER_{yy}(1:2:N_{2x}, 2:2:N_{2y}, 1:2:N_{2z}) \quad (3.94)$$

$$ER_{yz} = ER_{yz}(1:2:N_{2x}, 1:2:N_{2y}, 2:2:N_{2z}) \quad (3.95)$$

$$ER_{zx} = ER_{zx}(2:2:N_{2x}, 1:2:N_{2y}, 1:2:N_{2z}) \quad (3.96)$$

$$ER_{zy} = ER_{zy}(1:2:N_{2x}, 2:2:N_{2y}, 1:2:N_{2z}) \quad (3.97)$$

$$ER_{zz} = ER_{zz}(1:2:N_{2x}, 1:2:N_{2y}, 2:2:N_{2z}) \quad (3.98)$$

This can be seen more in depth in Ref [22]. The materials analyzed here have no magnetic response so their arrays do not get filled with any materials. However, you still have to initial the arrays associated with magnetic field quantities, like their electric counter parts as shown above, and then parse out the individual components. The same indexing process to separate terms works for both electric and

magnetic terms. The device and its parameters are ready to be modeled using either one of the following methods.

### 3.2 Surface Wave Analysis

To begin this section we have to make an assumption about the solution to our model. This assumption is that the modal solution is of the form dictated by the Bloch Theorem

$$\begin{aligned}\mathbf{e} &= \mathbf{a}(\tilde{x}, \tilde{y}) e^{-\gamma z/k_0} \\ \mathbf{h} &= \mathbf{b}(\tilde{x}, \tilde{y}) e^{-\gamma z/k_0}\end{aligned}\quad (3.99)$$

Arbitrarily choosing the axis of propagation along the  $z$ -axis, and substituting the assumed solution (3.99) back into the first equation of (3.33) results in equation (3.100).

$$\mathbf{D}_{\tilde{y}}^e(\mathbf{a}_x(\tilde{x}, \tilde{y}) e^{-\gamma z/k_0}) - \mathbf{D}_{\tilde{z}}^e(\mathbf{a}_y(\tilde{x}, \tilde{y}) e^{-\gamma z/k_0}) = \mu'_{rxx} \mathbf{b}_x(\tilde{x}, \tilde{y}) e^{-\gamma z/k_0} + \mu'_{rxy} \mathbf{b}_y(\tilde{x}, \tilde{y}) e^{-\gamma z/k_0} + \mu'_{rxz} \mathbf{b}_z(\tilde{x}, \tilde{y}) e^{-\gamma z/k_0} \quad (3.100)$$

Now evaluating the applicable differential terms yields

$$\mathbf{D}_{\tilde{y}}^e(\mathbf{a}_x(\tilde{x}, \tilde{y}) e^{-\gamma z/k_0}) + \frac{\gamma}{k_0} \mathbf{D}_{\tilde{z}}^e(\mathbf{a}_y(\tilde{x}, \tilde{y}) e^{-\gamma z/k_0}) = \mu'_{rxx} \mathbf{b}_x(\tilde{x}, \tilde{y}) e^{-\gamma z/k_0} + \mu'_{rxy} \mathbf{b}_y(\tilde{x}, \tilde{y}) e^{-\gamma z/k_0} + \mu'_{rxz} \mathbf{b}_z(\tilde{x}, \tilde{y}) e^{-\gamma z/k_0} \quad (3.101)$$

One can further reduce this equation by dividing out the  $e^{-\gamma z/k_0}$  term

$$\mathbf{D}_{\tilde{y}}^e \mathbf{a}_x + \frac{\gamma}{k_0} \mathbf{a}_y = \mu'_{rxx} \mathbf{b}_x + \mu'_{rxy} \mathbf{b}_y + \mu'_{rxz} \mathbf{b}_z \quad (3.102)$$

This same process is then applied to the other five equations in (3.32) and (3.33) resulting in the set of equations (3.103) and (3.104). The notation in these equations uses a normalized gamma operator,  $\tilde{\gamma} = \gamma/k_0$ , and matrix notation.

$$\begin{aligned}\mathbf{D}_{\tilde{y}}^e \mathbf{a}_z + \tilde{\gamma} \mathbf{a}_y &= \mu'_{rxx} \mathbf{b}_x + \mu'_{rxy} \mathbf{b}_y + \mu'_{rxz} \mathbf{b}_z \\ -\tilde{\gamma} \mathbf{a}_x - \mathbf{D}_{\tilde{x}}^e \mathbf{a}_z &= \mu'_{ryx} \mathbf{b}_x + \mu'_{ryy} \mathbf{b}_y + \mu'_{ryz} \mathbf{b}_z \\ \mathbf{D}_{\tilde{x}}^e \mathbf{a}_y - \mathbf{D}_{\tilde{y}}^e \mathbf{a}_x &= \mu'_{rxx} \mathbf{b}_x + \mu'_{ryy} \mathbf{b}_y + \mu'_{rzz} \mathbf{b}_z\end{aligned}\quad (3.103)$$

and

$$\begin{aligned}\mathbf{D}_{\tilde{y}}^h \mathbf{b}_z + \tilde{\gamma} \mathbf{b}_y &= \epsilon'_{rxx} \mathbf{a}_x + \epsilon'_{rxy} \mathbf{a}_y + \epsilon'_{rxz} \mathbf{a}_z \\ -\tilde{\gamma} \mathbf{b}_x - \mathbf{D}_{\tilde{x}}^h \mathbf{b}_z &= \epsilon'_{ryx} \mathbf{a}_x + \epsilon'_{ryy} \mathbf{a}_y + \epsilon'_{ryz} \mathbf{a}_z \\ \mathbf{D}_{\tilde{x}}^h \mathbf{b}_y - \mathbf{D}_{\tilde{y}}^h \mathbf{b}_x &= \epsilon'_{rxx} \mathbf{a}_x + \epsilon'_{ryy} \mathbf{a}_y + \epsilon'_{rzz} \mathbf{a}_z\end{aligned}\quad (3.104)$$

From these two sets of equations, the transverse components are isolated and shown in (3.105).

$$\begin{aligned} (\mathbf{D}_{\bar{x}}^e \mathbf{a}_y + \mathbf{D}_{\bar{y}}^e \mathbf{a}_x - \mu'_{zx} \mathbf{b}_x - \mu'_{zy} \mathbf{b}_y) \frac{1}{\mu'_{zz}} &= \mathbf{b}_z \\ (\mathbf{D}_{\bar{x}}^h \mathbf{b}_y + \mathbf{D}_{\bar{y}}^h \mathbf{b}_x - \epsilon'_{zx} \mathbf{a}_x - \epsilon'_{zy} \mathbf{a}_y) \frac{1}{\epsilon'_{zz}} &= \mathbf{a}_z \end{aligned} \quad (3.105)$$

The transverse components can then be inserted back into equation (3.103) resulting in

$$\begin{aligned} \tilde{\gamma} \mathbf{a}_y &= \epsilon'_{zx} \frac{1}{\epsilon'_{zz}} \mathbf{D}_{\bar{y}}^e \mathbf{a}_x - \mu'_{xz} \frac{1}{\mu'_{zz}} \mathbf{D}_{\bar{y}}^e \mathbf{a}_x + \epsilon'_{zy} \frac{1}{\epsilon'_{zz}} \mathbf{D}_{\bar{x}}^e \mathbf{a}_y + \mu'_{xz} \frac{1}{\mu'_{zz}} \mathbf{D}_{\bar{x}}^e \mathbf{a}_y \\ &\quad - \mu'_{xz} \frac{1}{\mu'_{zz}} \mu'_{zx} \mathbf{b}_x + \mu'_{xx} \mathbf{b}_x - \frac{1}{\epsilon'_{zz}} \mathbf{D}_{\bar{y}}^e \mathbf{D}_{\bar{y}}^h \mathbf{b}_x - \mu'_{xz} \frac{1}{\mu'_{zz}} \mu'_{zy} \mathbf{b}_y + \mu'_{xy} \mathbf{b}_y - \frac{1}{\epsilon'_{zz}} \mathbf{D}_{\bar{y}}^e \mathbf{D}_{\bar{x}}^h \mathbf{b}_y \\ \tilde{\gamma} \mathbf{a}_x &= -\mu'_{yz} \frac{1}{\mu'_{zz}} \mathbf{D}_{\bar{y}}^e \mathbf{a}_x + \frac{1}{\epsilon'_{zz}} \epsilon'_{zx} \mathbf{D}_{\bar{x}}^e \mathbf{a}_x - \mu'_{yz} \frac{1}{\mu'_{zz}} \mathbf{D}_{\bar{x}}^e \mathbf{a}_y + \frac{1}{\epsilon'_{zz}} \epsilon'_{zy} \mathbf{D}_{\bar{x}}^e \mathbf{a}_y \\ &\quad - \mu'_{yx} \mathbf{b}_x + \frac{1}{\epsilon'_{zz}} \mathbf{D}_{\bar{x}}^e \mathbf{D}_{\bar{y}}^h \mathbf{b}_x + \mu'_{yz} \frac{1}{\mu'_{zz}} \mu'_{zx} \mathbf{b}_x + \mu'_{yz} \frac{1}{\mu'_{zz}} \mu'_{zy} \mathbf{b}_y - \mu'_{yy} \mathbf{b}_y - \frac{1}{\epsilon'_{zz}} \mathbf{D}_{\bar{x}}^e \mathbf{D}_{\bar{x}}^h \mathbf{b}_y \end{aligned} \quad (3.106)$$

This same process is then applied to equations (3.105)

$$\begin{aligned} \tilde{\gamma} \mathbf{b}_y &= \frac{1}{\mu'_{zz}} \mathbf{D}_{\bar{y}}^h \mathbf{D}_{\bar{y}}^e \mathbf{a}_x + \epsilon'_{xx} \mathbf{a}_x - \epsilon'_{xz} \frac{1}{\epsilon'_{zz}} \epsilon'_{zx} \mathbf{a}_x + \epsilon'_{xy} \mathbf{a}_y - \epsilon'_{xz} \frac{1}{\epsilon'_{zz}} \epsilon'_{zy} \mathbf{a}_y - \frac{1}{\mu'_{zz}} \mathbf{D}_{\bar{y}}^h \mathbf{D}_{\bar{x}}^e \mathbf{a}_y \\ &\quad + \frac{1}{\mu'_{zz}} \mu'_{zx} \mathbf{D}_{\bar{y}}^h \mathbf{b}_x - \epsilon'_{xz} \frac{1}{\epsilon'_{zz}} \mathbf{D}_{\bar{y}}^h \mathbf{b}_x + \frac{1}{\mu'_{zz}} \mu'_{zy} \mathbf{D}_{\bar{y}}^h \mathbf{b}_y + \epsilon'_{xz} \frac{1}{\epsilon'_{zz}} \mathbf{D}_{\bar{x}}^h \mathbf{b}_y \\ \tilde{\gamma} \mathbf{b}_x &= \epsilon'_{yz} \frac{1}{\epsilon'_{zz}} \epsilon'_{zx} \mathbf{a}_x - \epsilon'_{yx} \mathbf{a}_x - \frac{1}{\mu'_{zz}} \mathbf{D}_{\bar{x}}^h \mathbf{D}_{\bar{y}}^e \mathbf{a}_x - \frac{1}{\mu'_{zz}} \mathbf{D}_{\bar{x}}^h \mathbf{D}_{\bar{x}}^e \mathbf{a}_y + \epsilon'_{yz} \frac{1}{\epsilon'_{zz}} \epsilon'_{zy} \mathbf{a}_y - \epsilon'_{yy} \mathbf{a}_y \\ &\quad + \epsilon'_{yz} \frac{1}{\epsilon'_{zz}} \mathbf{D}_{\bar{y}}^h \mathbf{b}_x + \frac{1}{\mu'_{zz}} \mu'_{zx} \mathbf{D}_{\bar{x}}^h \mathbf{b}_x + \frac{1}{\mu'_{zz}} \mu'_{zy} \mathbf{D}_{\bar{x}}^h \mathbf{b}_y - \epsilon'_{yz} \frac{1}{\epsilon'_{zz}} \mathbf{D}_{\bar{x}}^h \mathbf{b}_y \end{aligned} \quad (3.107)$$

The four equations in (3.106) and (3.107) describe the field components associated with the modes that propagate in the surface wave analysis. They will describe the hybrid waves that propagate in the interface of an anisotropic crystal and isotropic cladding. This four equations can be arrange in a matrix depicting an eigenvalue problem of the form

$$\mathbf{A} \mathbf{x} = \gamma \mathbf{x} \rightarrow \begin{bmatrix} \mathbf{a}_{11} & \mathbf{a}_{12} & \mathbf{a}_{13} & \mathbf{a}_{14} \\ \mathbf{a}_{21} & \mathbf{a}_{22} & \mathbf{a}_{23} & \mathbf{a}_{24} \\ \mathbf{a}_{31} & \mathbf{a}_{32} & \mathbf{a}_{33} & \mathbf{a}_{34} \\ \mathbf{a}_{41} & \mathbf{a}_{42} & \mathbf{a}_{43} & \mathbf{a}_{44} \end{bmatrix} \begin{bmatrix} a_x \\ a_y \\ b_x \\ b_y \end{bmatrix} = \gamma \mathbf{x} \quad (3.108)$$

The elements of  $\mathbf{A}$  are the grouped terms associated with each field components  $a_x, a_y, b_x$  and  $b_y$  in equations (3.106) and (3.107). The elements of  $\mathbf{A}$  are

$$\begin{aligned}
\mathbf{a}_{11} &= \epsilon'_{rxz} \frac{1}{\epsilon'_{rzz}} \mathbf{D}_{\tilde{y}}^e - \mu'_{rxz} \frac{1}{\mu'_{rzz}} \mathbf{D}_{\tilde{y}}^e, \quad \mathbf{a}_{12} = -\mu'_{ryz} \frac{1}{\mu'_{rzz}} \mathbf{D}_{\tilde{x}}^e + \frac{1}{\epsilon'_{rzz}} \epsilon'_{rzy} \mathbf{D}_{\tilde{x}}^e, \\
\mathbf{a}_{13} &= -\mu'_{ryx} + \frac{1}{\epsilon'_{rzz}} \mathbf{D}_{\tilde{x}}^e \mathbf{D}_{\tilde{y}}^h + \mu'_{ryz} \frac{1}{\mu'_{rzz}} \mu'_{rxz}, \quad \mathbf{a}_{14} = \mu'_{ryz} \frac{1}{\mu'_{rzz}} \mu'_{rzy} - \mu'_{ryy} - \frac{1}{\epsilon'_{rzz}} \mathbf{D}_{\tilde{x}}^e \mathbf{D}_{\tilde{x}}^h \\
\mathbf{a}_{21} &= \epsilon'_{rxz} \frac{1}{\epsilon'_{rzz}} \mathbf{D}_{\tilde{y}}^e - \mu'_{rxz} \frac{1}{\mu'_{rzz}} \mathbf{D}_{\tilde{y}}^e, \quad \mathbf{a}_{22} = \epsilon'_{rzy} \frac{1}{\epsilon'_{rzz}} \mathbf{D}_{\tilde{y}}^e + \mu'_{rxz} \frac{1}{\mu'_{rzz}} \mathbf{D}_{\tilde{x}}^e, \\
\mathbf{a}_{23} &= -\mu'_{rxz} \frac{1}{\mu'_{rzz}} \mu'_{rxz} + \mu'_{rxz} - \frac{1}{\epsilon'_{rzz}} \mathbf{D}_{\tilde{y}}^e \mathbf{D}_{\tilde{y}}^h, \quad \mathbf{a}_{24} = -\mu'_{rxz} \frac{1}{\mu'_{rzz}} \mu'_{rzy} + \mu'_{rxy} - \frac{1}{\epsilon'_{rzz}} \mathbf{D}_{\tilde{y}}^e \mathbf{D}_{\tilde{x}}^h \\
\mathbf{a}_{31} &= \epsilon'_{ryz} \frac{1}{\epsilon'_{rzz}} \epsilon'_{rxz} - \epsilon'_{ryx} - \frac{1}{\mu'_{rzz}} \mathbf{D}_{\tilde{x}}^h \mathbf{D}_{\tilde{y}}^e, \quad \mathbf{a}_{32} = -\frac{1}{\mu'_{rzz}} \mathbf{D}_{\tilde{x}}^h \mathbf{D}_{\tilde{x}}^e + \epsilon'_{ryz} \frac{1}{\epsilon'_{rzz}} \epsilon'_{rzy} - \epsilon'_{ryy} \\
\mathbf{a}_{33} &= \epsilon'_{ryz} \frac{1}{\epsilon'_{rzz}} \mathbf{D}_{\tilde{y}}^h + \frac{1}{\mu'_{rzz}} \mu'_{rxz} \mathbf{D}_{\tilde{x}}^h, \quad \mathbf{a}_{34} = \frac{1}{\mu'_{rzz}} \mu'_{rzy} \mathbf{D}_{\tilde{x}}^h - \epsilon'_{ryz} \frac{1}{\epsilon'_{rzz}} \mathbf{D}_{\tilde{x}}^h \\
\mathbf{a}_{41} &= \frac{1}{\mu'_{rzz}} \mathbf{D}_{\tilde{y}}^h \mathbf{D}_{\tilde{y}}^e + \epsilon'_{rxz} - \epsilon'_{rxz} \frac{1}{\epsilon'_{rzz}} \epsilon'_{rxz}, \quad \mathbf{a}_{42} = \epsilon'_{rxy} - \epsilon'_{rxz} \frac{1}{\epsilon'_{rzz}} \epsilon'_{rzy} - \frac{1}{\mu'_{rzz}} \mathbf{D}_{\tilde{y}}^h \mathbf{D}_{\tilde{x}}^e, \\
\mathbf{a}_{43} &= \frac{1}{\mu'_{rzz}} \mu'_{rxz} \mathbf{D}_{\tilde{y}}^h - \epsilon'_{rxz} \frac{1}{\epsilon'_{rzz}} \mathbf{D}_{\tilde{y}}^h, \quad \mathbf{a}_{44} = \frac{1}{\mu'_{rzz}} \mu'_{rzy} \mathbf{D}_{\tilde{y}}^h + \epsilon'_{rxz} \frac{1}{\epsilon'_{rzz}} \mathbf{D}_{\tilde{x}}^h
\end{aligned}$$

The equations governing propagation in X and then Y directions, are presented below. The set of equations that compose matrix  $\mathbf{A}$  for X-axis propagation are

$$\begin{aligned}
\mathbf{a}_y &= \mu'_{rx} \frac{1}{\mu'_{rxx}} \mathbf{D}_z^e \mathbf{a}_y + \frac{1}{\epsilon'_{rxx}} \epsilon'_{rxy} \mathbf{D}_y^e \mathbf{a}_y + \frac{1}{\epsilon'_{rxx}} \epsilon'_{rxz} \mathbf{D}_y^e \mathbf{a}_z - \mu'_{rx} \frac{1}{\mu'_{rxx}} \mathbf{D}_y^e \mathbf{a}_z \\
&\quad + \mu'_{rx} \frac{1}{\mu'_{rxx}} \mu'_{rxy} \mathbf{b}_y - \mu'_{rxy} \mathbf{b}_y + \frac{1}{\epsilon'_{rxx}} \mathbf{D}_y^e \mathbf{D}_z^h \mathbf{b}_y + \mu'_{rx} \frac{1}{\mu'_{rxx}} \mu'_{rxz} \mathbf{b}_z - \mu'_{rzz} \mathbf{b}_z + \frac{1}{\epsilon'_{rxx}} \mathbf{D}_y^e \mathbf{D}_y^h \mathbf{b}_z \\
\mathbf{a}_z &= -\mu'_{ryx} \frac{1}{\mu'_{rxx}} \mathbf{D}_z^e \mathbf{a}_y + \frac{1}{\epsilon'_{rxx}} \epsilon'_{rxy} \mathbf{D}_z^e \mathbf{a}_y + \frac{1}{\epsilon'_{rxx}} \epsilon'_{rxz} \mathbf{D}_z^e \mathbf{a}_z + \mu'_{ryx} \frac{1}{\mu'_{rxx}} \mathbf{D}_y^e \mathbf{a}_z \\
&\quad - \mu'_{ryx} \frac{1}{\mu'_{rxx}} \mu'_{rxy} \mathbf{b}_y + \mu'_{ryy} \mathbf{b}_y + \frac{1}{\epsilon'_{rxx}} \mathbf{D}_z^e \mathbf{D}_z^h \mathbf{b}_y - \mu'_{ryx} \frac{1}{\mu'_{rxx}} \mu'_{rxz} \mathbf{b}_z + \mu'_{ryz} \mathbf{b}_z - \frac{1}{\epsilon'_{rxx}} \mathbf{D}_z^e \mathbf{D}_y^h \mathbf{b}_z \\
\mathbf{b}_y &= \epsilon'_{rx} \frac{1}{\epsilon'_{rxx}} \epsilon'_{rxy} \mathbf{a}_y - \epsilon'_{rxy} \mathbf{a}_y + \frac{1}{\mu'_{rxx}} \mathbf{D}_y^h \mathbf{D}_z^e \mathbf{a}_y - \epsilon_{rzz} \mathbf{a}_z + \epsilon_{rx} \frac{1}{\epsilon_{rxx}} \epsilon_{rxz} \mathbf{a}_z \\
&\quad - \frac{1}{\mu'_{rxx}} \mathbf{D}_y^h \mathbf{D}_y^e \mathbf{a}_z + \epsilon'_{rx} \frac{1}{\epsilon'_{rxx}} \mathbf{D}_z^h \mathbf{b}_y + \frac{1}{\mu'_{rxx}} \mu'_{rxy} \mathbf{D}_y^h \mathbf{b}_y + \frac{1}{\mu_{rxx}} \mu_{rxz} \mathbf{D}_y^h \mathbf{b}_z - \epsilon_{rx} \frac{1}{\epsilon_{rxx}} \mathbf{D}_y^h \mathbf{b}_z \\
\mathbf{b}_z &= -\epsilon'_{ryx} \frac{1}{\epsilon'_{rxx}} \epsilon'_{rxy} \mathbf{a}_y + \epsilon'_{ryy} \mathbf{a}_y + \frac{1}{\mu'_{rxx}} \mathbf{D}_z^h \mathbf{D}_z^e \mathbf{a}_y - \epsilon'_{ryx} \frac{1}{\epsilon'_{rxx}} \epsilon'_{rxz} \mathbf{a}_z + \epsilon'_{ryz} \mathbf{a}_z \\
&\quad - \frac{1}{\mu'_{rxx}} \mathbf{D}_z^h \mathbf{D}_y^e \mathbf{a}_z - \epsilon'_{ryx} \frac{1}{\epsilon'_{rxx}} \mathbf{D}_z^h \mathbf{b}_y + \frac{1}{\mu'_{rxx}} \mu'_{rxy} \mathbf{D}_z^h \mathbf{b}_y + \frac{1}{\mu'_{rxx}} \mu'_{rxz} \mathbf{D}_z^h \mathbf{b}_z + \epsilon'_{ryx} \frac{1}{\epsilon'_{rxx}} \mathbf{D}_y^h \mathbf{b}_z
\end{aligned} \tag{3.109}$$

### In the case of propagation along Y-axis

$$\begin{aligned}
\mathbf{a}_x &= \mu'_{rxy} \frac{1}{\mu'_{rxy}} \mathbf{D}_z^e \mathbf{a}_x + \frac{1}{\epsilon'_{rxy}} \epsilon'_{rxy} \mathbf{D}_x^e \mathbf{a}_x + \frac{1}{\epsilon'_{rxy}} \epsilon'_{rxy} \mathbf{D}_x^e \mathbf{a}_z - \mu'_{rxy} \frac{1}{\mu'_{rxy}} \mathbf{D}_x^e \mathbf{a}_z \\
&+ \mu'_{rxz} \mathbf{b}_x - \mu'_{rxy} \frac{1}{\mu'_{rxy}} \mu'_{rxy} \mathbf{b}_x - \frac{1}{\epsilon'_{rxy}} \mathbf{D}_x^e \mathbf{D}_z^h \mathbf{b}_x - \mu'_{rxy} \frac{1}{\mu'_{rxy}} \mu'_{rxy} \mathbf{b}_z + \mu'_{rzz} \mathbf{b}_z + \frac{1}{\epsilon'_{rxy}} \mathbf{D}_x^e \mathbf{D}_x^h \mathbf{b}_z \\
\mathbf{a}_z &= -\mu'_{rxy} \frac{1}{\mu'_{rxy}} \mathbf{D}_z^e \mathbf{a}_x + \frac{1}{\epsilon'_{rxy}} \epsilon'_{rxy} \mathbf{D}_z^e \mathbf{a}_x + \frac{1}{\epsilon'_{rxy}} \epsilon'_{rxy} \mathbf{D}_z^e \mathbf{a}_z + \mu'_{rxy} \frac{1}{\mu'_{rxy}} \mathbf{D}_x^e \mathbf{a}_z \\
&+ \mu'_{rxy} \frac{1}{\mu'_{rxy}} \mu'_{rxy} \mathbf{b}_x - \mu'_{rxy} \mathbf{b}_x - \frac{1}{\epsilon'_{rxy}} \mathbf{D}_z^e \mathbf{D}_z^h \mathbf{b}_x + \mu'_{rxy} \frac{1}{\mu'_{rxy}} \mu'_{rxy} \mathbf{b}_z - \mu'_{rxz} \mathbf{b}_z + \frac{1}{\epsilon'_{rxy}} \mathbf{D}_z^e \mathbf{D}_x^h \mathbf{b}_z \\
\mathbf{b}_x &= \epsilon'_{rxz} \mathbf{a}_x - \epsilon'_{rxy} \frac{1}{\epsilon'_{rxy}} \epsilon'_{rxy} \mathbf{a}_x - \frac{1}{\mu'_{rxy}} \mathbf{D}_x^h \mathbf{D}_z^e \mathbf{a}_x - \epsilon'_{rxy} \frac{1}{\epsilon'_{rxy}} \epsilon'_{rxy} \mathbf{a}_z + \epsilon'_{rzz} \mathbf{a}_z \\
&+ \frac{1}{\mu'_{rxy}} \mathbf{D}_x^h \mathbf{D}_x^e \mathbf{a}_z + \epsilon'_{rxy} \frac{1}{\epsilon'_{rxy}} \mathbf{D}_z^h \mathbf{b}_x + \frac{1}{\mu'_{rxy}} \mu'_{rxy} \mathbf{D}_x^h \mathbf{b}_x + \frac{1}{\mu'_{rxy}} \mu'_{rxy} \mathbf{D}_x^h \mathbf{b}_z - \epsilon'_{rxy} \frac{1}{\epsilon'_{rxy}} \mathbf{D}_x^h \mathbf{b}_z \\
\mathbf{b}_z &= -\frac{1}{\mu'_{rxy}} \mathbf{D}_z^h \mathbf{D}_z^e \mathbf{a}_x - \epsilon'_{rxz} \mathbf{a}_x + \epsilon'_{rxy} \frac{1}{\epsilon'_{rxy}} \epsilon'_{rxy} \mathbf{a}_x + \frac{1}{\mu'_{rxy}} \mathbf{D}_z^h \mathbf{D}_x^e \mathbf{a}_z + \epsilon'_{rxy} \frac{1}{\epsilon'_{rxy}} \epsilon'_{rxy} \mathbf{a}_z \\
&- \epsilon'_{rxz} \mathbf{a}_z - \epsilon'_{rxy} \frac{1}{\epsilon'_{rxy}} \mathbf{D}_z^h \mathbf{b}_x + \frac{1}{\mu'_{rxy}} \mu'_{rxy} \mathbf{D}_z^h \mathbf{b}_x + \frac{1}{\mu'_{rxy}} \mu'_{rxy} \mathbf{D}_z^h \mathbf{b}_z + \epsilon'_{rxy} \frac{1}{\epsilon'_{rxy}} \mathbf{D}_x^h \mathbf{b}_z
\end{aligned} \tag{3.110}$$

At this point one now has the ability to determine the surface modes in the surface wave analysis tool. The modes are only half of the results produced by Eigen value problem. The Eigen problem produces a matrix of Eigen vectors, the surface modes, and a column vector of Eigen values, which are the un-normalized propagation terms, associated with each mode. The values in the column vector are complex and have the form  $\gamma = \alpha - j\beta$ . The term  $\alpha$ , alpha, is the attenuation term, which describes the rate at which the amplitude of the wave decays. The term  $\beta$ , beta, describes rate at which the wave accumulates phase and can be isolated by taking the imaginary portion of gamma  $\beta = \text{Im}(\gamma)$ . A more meaningful quantity would be the effective refractive index because that is one of primary ways materials or devices are characterized. The refractive index can be derived from  $\beta$ . The propagation constant can be written as  $\beta = k_0 n_{eff}$ . Rearranging for the effective refractive index gives  $n_{eff} = \beta/k_0$ . Since only one Dyakonov surface mode can exist at a time the largest effective refractive index and the associated Eigen vector describe the DSW.

### 3.3 3D Anisotropic FDFD for Scattering Analysis

The next portion of the algorithm provides the means to model an anisotropic material or device as scattering problem. This requires the use of source to excite device fields in the device under question and will be address shortly. The first step in the scattering analysis is declaring the field components (3.111) and curl operators as the set of equations (3.112)

$$\mathbf{e} = \begin{bmatrix} \mathbf{e}_x \\ \mathbf{e}_y \\ \mathbf{e}_z \end{bmatrix} \quad \mathbf{h} = \begin{bmatrix} \mathbf{h}_x \\ \mathbf{h}_y \\ \mathbf{h}_z \end{bmatrix} \quad (3.111)$$

$$\mathbf{C}^h = \begin{bmatrix} \mathbf{0} & -\mathbf{D}_z^h & \mathbf{D}_y^h \\ \mathbf{D}_z^h & \mathbf{0} & -\mathbf{D}_x^h \\ -\mathbf{D}_y^h & \mathbf{D}_x^h & \mathbf{0} \end{bmatrix} \quad \mathbf{C}^e = \begin{bmatrix} \mathbf{0} & -\mathbf{D}_z^e & \mathbf{D}_y^e \\ \mathbf{D}_z^e & \mathbf{0} & -\mathbf{D}_x^e \\ -\mathbf{D}_y^e & \mathbf{D}_x^e & \mathbf{0} \end{bmatrix} \quad (3.112)$$

The matrices in (3.113) are block matrices that describe the permittivity and permeability through out the entire grid. Each element of these block matrices is a diagonal matrix describing the permittivity or permeability through out the grid as previously mentioned in the surface wave analysis.

$$\mu = \begin{bmatrix} \mu'_{rxx} & \mu'_{rxy} & \mu'_{rxz} \\ \mu'_{ryx} & \mu'_{ryy} & \mu'_{ryz} \\ \mu'_{rzx} & \mu'_{rzy} & \mu'_{rzz} \end{bmatrix} \quad \varepsilon = \begin{bmatrix} \varepsilon'_{rxx} & \varepsilon'_{rxy} & \varepsilon'_{rxz} \\ \varepsilon'_{ryx} & \varepsilon'_{ryy} & \varepsilon'_{ryz} \\ \varepsilon'_{rzx} & \varepsilon'_{rzy} & \varepsilon'_{rzz} \end{bmatrix} \quad (3.113)$$

These three systems can be combined to form the system of equations  $A$  or better known as the wave equation in

$$\mathbf{A}\mathbf{h} = 0 \quad \text{with} \quad \mathbf{A} = \mathbf{C}^e [\boldsymbol{\varepsilon}]^{-1} \mathbf{C}^h - [\boldsymbol{\mu}] \quad (3.114)$$

and

$$\mathbf{A}\mathbf{e} = 0 \quad \text{with} \quad \mathbf{A} = \mathbf{C}^h [\boldsymbol{\mu}]^{-1} \mathbf{C}^e - [\boldsymbol{\varepsilon}] \quad (3.115)$$

Before proceeding to solve our system of linear equations we choose to implement the Transparent Boundary Condition to alleviate time and computing power required for computation [23]. This is a good boundary condition to partner with the UPML as it allows the method to handle the large evanescent fields with smaller spacer regions causing a reduction in computational time. This boundary condition is summarized in three large steps. First, you reorder the wave matrix, so that the grid elements that describe the electric or magnetic field are grouped together with respect to the axis they describe. Next, use a propagator matrix to estimate the fields outside of the grid and as the last step you re-incorporate the extrapolated field values back into the grid as the new boundary condition.

### 3.3.1 Transparent Boundary Condition

The very first step is to take the vector describing field components of each axis  $x$ ,  $y$ , and  $z$  along the grid and reorder it. This means that we rearrange the field components such that they become grouped by their respective axis. For illustrative purposes we take the matrix,  $X$ , which is an  $n$  by  $m$  matrix describing the locations of the grid components, and make it a column vector, of length  $p$  where  $p = n * m$ .

$$X = \begin{bmatrix} x_{x,1} \\ x_{y,1} \\ x_{z,1} \\ x_{x,2} \\ x_{y,2} \\ x_{z,2} \\ \vdots \\ x_{x,p} \\ x_{y,p} \\ x_{z,p} \end{bmatrix} \quad (3.116)$$

When we order it, the vector becomes.

$$X = \begin{bmatrix} x_{x,1} \\ \vdots \\ x_{x,p} \\ x_{y,1} \\ \vdots \\ x_{y,p} \\ x_{z,1} \\ \vdots \\ x_{z,p} \end{bmatrix} \quad (3.117)$$

The second index denotes the cell associated to that field coefficient. This vector acts on the wave matrix  $A$ . This means that the elements in the wave matrix  $A$  need to be reordered to remain consistent with the respective field components.

The next step involves the construction of the propagator matrix,  $P$ , which is a product of three matrices. These matrices are the tilt operator  $T$ , a discrete Fourier transform operator,  $Ft$ , and a phase accumulation matrix  $[Z]$ . The tilt operator removes the phase tilt associated with oblique incidence. The next step performs a Fourier transform by multiplying the  $Ft$  operator, which computes the plane wave spectrum of harmonics. The last portion advances these harmonics by the phase accumulation dictated by the matrix  $[Z]$ . After all prior operations have been performed, the field is then reconstructed by



applying the inverse Fourier transform and incorporating the phase tilt was initially removed. All together the propagator for the transmission side is

$$\mathbf{P}_{trn}^e = (\mathbf{T} \cdot \mathbf{Ft})^{-1} \mathbf{Z}_{trn} (\mathbf{T} \cdot \mathbf{Ft}) \quad (3.118)$$

and for the reflected side

$$\mathbf{P}_{ref}^e = (\mathbf{T} \cdot \mathbf{Ft})^{-1} \mathbf{Z}_{ref} (\mathbf{T} \cdot \mathbf{Ft}) \quad (3.119)$$

The elements of  $\mathbf{T}$  are defined from the equation  $t = e^{j(k_{x,inc} \cdot X + k_{y,inc} \cdot Y)}$  where matrices  $\mathbf{X}$ , and  $\mathbf{Y}$  contain the transverse grid components through out the grid. The tilt operator is also reordered and results in

$$\mathbf{T} = \begin{bmatrix} \mathbf{t} & \mathbf{0} & \mathbf{0} \\ \mathbf{0} & \mathbf{t} & \mathbf{0} \\ \mathbf{0} & \mathbf{0} & \mathbf{t} \end{bmatrix} \quad (3.120)$$

The next operator performs a 2D discrete Fourier transform using the form

$$\vec{L}(m,n) = \sum_p \sum_q \vec{l}(p,q) e^{-j2\pi[(mp/M)+(nq/N)]} \quad (3.121)$$

The variables  $L$  and  $l$  are column vectors containing scalar values used by the functions  $L(m,n)$  and  $l(p,q)$  respectfully. This equation describes the variable  $f$  in the system  $L = \dot{F}l$ . The final transform matrix is build as

$$\mathbf{Ft} = \begin{bmatrix} \dot{\mathbf{F}} & \mathbf{0} & \mathbf{0} \\ \mathbf{0} & \dot{\mathbf{F}} & \mathbf{0} \\ \mathbf{0} & \mathbf{0} & \dot{\mathbf{F}} \end{bmatrix} \quad (3.122)$$

The final step is to incorporate these operators back into the grid at the designated areas by applying the appropriate  $[\mathbf{P}]$  operator to each individual element in the transmitted and reflected regions.

### 3.3.2 Solving the Matrix Wave Equation

Our sets of equations are still in the form of  $Ax=0$ , however, this provides only trivial solutions. In order to find a non-trivial solution a source must be built and then incorporated into the wave equation. A simple example of a source would be a plane wave and its generic form is

$$E_{src}(\vec{r}) = e^{jk_{inc} \cdot \vec{r}} \quad (3.123)$$

Here  $\vec{r}$  is the position vector, which when expanded is  $\vec{r} = x \cdot \hat{x} + y \cdot \hat{y} + z \cdot \hat{z}$  for three dimensions. In order to interpret meaningful data from the simulation the waves scattered by the device must be isolated from the incoming waves. This allows the user to tell the difference between reflected and incident power. There is a simple and elegant solution to this type of problem and that is the implementation of a method known as the total-field/scattered-field [19]. It is popular for incorporating sources into electromagnetic modeling. By incorporating this methodology, we can separate the total-field, the field with both incoming and reflected waves, from the scattered-field region, which are the purely scattered waves. In the image below, Figure 3.3 shows a device that is assumed to be periodic, on the left and right, but from the top and bottom it is characterized by a UPML. Between the UPML and the device sits a boundary in the top portion of the image, marked by the solid red line. This red line designates to interface of the scatter-field (SF) from the total-field (TF) quantities.

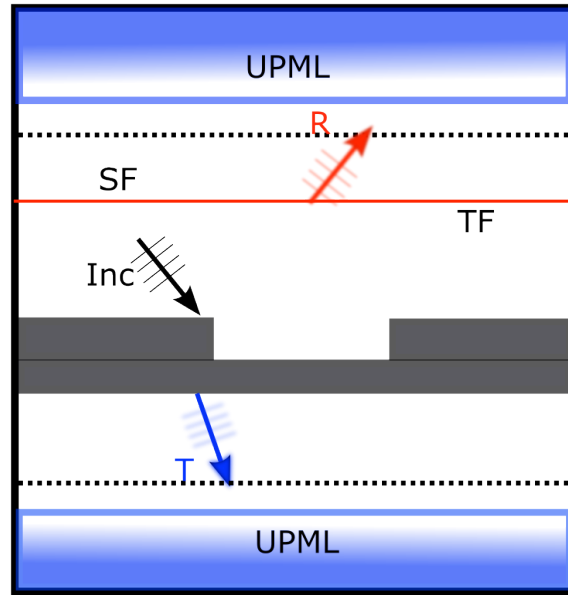


Figure 3.3 TF/SF Sample Configuration

Waves scattered back by the device interface are free to pass through this interface, where they are recorded, and enter the SF region of the grid. The two dotted lines, labeled by a T and R, signify the areas where field amplitude measurements for transmission and reflection are calculated.

By laying out the models this way, the separation between the regions governing scattered waves from those dealing with total/incident field interactions is much clearer. To actually implement this

method, you must first create both a source vector and masking matrix. Their matrix sizes will encompass the entire grid. The source field is calculated without taking the device structure into consideration so that the result is smooth and continuous everywhere. This source matrix is then reshaped into a column vector.

$$\mathbf{F}_{src} = \begin{bmatrix} f_{src}^{1,1} \\ f_{src}^{2,1} \\ \vdots \\ f_{src}^{Nx-1,Ny-1} \\ f_{src}^{Nx,Ny} \end{bmatrix} \quad (3.124)$$

The masking matrix  $\mathbf{Q}$  uses ones and zeros to dictate where the scattered and total field quantities reside. Ones represent scattered-field values and zeros are for total-field quantities. These ones and zeros are placed down the main diagonal of a sparse matrix  $\mathbf{Q}$ . An example of  $\mathbf{Q}$  could be

$$\mathbf{Q} = \begin{bmatrix} 0 & & & & & \\ & 1 & & & & \\ & & 1 & & & \\ & & & 0 & & \\ & & & & \ddots & \\ & & & & & 0 \end{bmatrix} \quad (3.125)$$

The ones and zeros here are distributed randomly for illustrative purposes. Using the masking matrix and an identity matrix of equal dimensioning one can now mathematically separate the different quantities in our model. The SF can be isolated as

$$\mathbf{f}_{SF} = \mathbf{Q}\mathbf{f}_{src} \quad (3.126)$$

and the total-field isolated as

$$\mathbf{f}_{TF} = (\mathbf{I} - \mathbf{Q})\mathbf{f}_{src} \quad (3.127)$$

However as we use these equations through out the entire grid there becomes a problematic area where field quantities are characterized by both scattered-field and total-field values. This area is at the boundary of the total-field/scattered-field interface. These equations must be fixed so that they are composed entirely of TF or SF depending on which region they are defined. To correct the TF terms in the SF region we subtract the TF terms out using the masking matrix. This accomplished by using

$\mathbf{Q}\mathbf{A}\mathbf{f}_{\text{TF}}$ . To remove the SF terms in the TF region we add the SF terms using  $(\mathbf{I} - \mathbf{Q})\mathbf{A}\mathbf{f}_{\text{SF}}$ . These two quantities are then incorporated with our wave equation A, resulting in

$$\mathbf{A}\mathbf{x} - \mathbf{Q}\mathbf{A}\mathbf{f}_{\text{TF}} + (\mathbf{I} - \mathbf{Q})\mathbf{A}\mathbf{f}_{\text{SF}} = 0 \quad (3.128)$$

The correction terms can be brought to the right hand side and then simplified to

$$\mathbf{A}\mathbf{x} = \mathbf{b} \quad (3.129)$$

The source  $\mathbf{b}$  is now defined as

$$\mathbf{b} = (\mathbf{Q}\mathbf{A} - \mathbf{A}\mathbf{Q})\mathbf{f}_{\text{src}} \quad (3.130)$$

The term  $\mathbf{b}$  is now our source vector used to solve the set of linear equations formed by (3.129).

Now that we have a non-trivial solution to our system we must devise a way to interpret these results in more meaningful ways. One useful way to post-process the field data is to calculate transmission and reflection by integrating the Poynting vector. This can also be accomplished by calculating the amplitudes of the diffracted order in the plane wave spectrum associated within the regions of the transmission and reflection record planes. These diffracted orders are a result of the source interacting with a periodic structure, the device being simulated, and separating into an infinite set of plane waves, all at different angles. Only a select few of these diffracted orders propagate power away from the point of interaction and are recorded as the fields,  $A$ , in the transmission and reflection areas. To calculate just how much power each wave carries the phase tilt associated with an oblique angle of incidence has to be removed. The fields in the transmission and reflection regions have the form

$$\mathbf{A} = \begin{bmatrix} \mathbf{E}_x \\ \mathbf{E}_y \\ \mathbf{E}_z \end{bmatrix}$$

To remove the tilt of the fields in the transmission region, you would divide out phase tilt  $\phi(x) = e^{-jk_{x,\text{inc}}x}$  as shown

$$\mathbf{A}_{\text{tn}} = \frac{\mathbf{E}_{z,\text{tn}}(x,y)}{\phi(x)} \quad (3.131)$$

The same process could then be applied to the fields for the reflectance region

$$\mathbf{A}_{ref} = \frac{\mathbf{E}_{z,ref}(x,y)}{\phi(x)} \quad (3.132)$$

Now that the fields are isolated, you can obtain amplitudes of each diffraction order, represented by  $S$ , using the Fourier Transform.

$$\mathbf{S}_{trn}(m) = FFT(\mathbf{A}_{trn}(m)) \quad (3.133)$$

and

$$\mathbf{S}_{ref}(m) = FFT(\mathbf{A}_{ref}(m)) \quad (3.134)$$

The index  $m$  specifies which diffraction component is being evaluated. It would also be very beneficial to find the over all transmitted and reflected power of the system. However, to do so, you have to relate these amplitudes to the source. This requires knowledge of the wave vector components that carry power away from the device.

$$\begin{aligned} \mathbf{k}_x^2 &= \sqrt{\mu_{inc,i}/\epsilon_{inc,i}} \sin(\theta) \cos(\phi) \\ \mathbf{k}_y^2 &= \sqrt{\mu_{inc,i}/\epsilon_{inc,i}} \sin(\theta) \sin(\phi) \end{aligned} \quad (3.135)$$

$$\begin{aligned} \mathbf{k}_{z,trn} &= conj\left(\sqrt{\mu_{r,i}/\epsilon_{r,i} - \mathbf{k}_x^2 - \mathbf{k}_y^2}\right) \\ \mathbf{k}_{z,ref} &= conj\left(\sqrt{\mu_{r,i}/\epsilon_{r,i} - \mathbf{k}_x^2 - \mathbf{k}_y^2}\right) \end{aligned} \quad (3.136)$$

For a given source amplitude  $S_{inc}$ , the power of the transmitted and reflected fields are found by

$$T_e(m) = \frac{|S_{trn}(m)|^2}{|S_{inc}|^2} \text{Re} \left[ \frac{\mathbf{k}_{z,m}^{trn} \cdot \mu_{r,inc}}{\mathbf{k}_z^{inc} \cdot \mu_{r,trn}} \right] \quad (3.137)$$

and

$$R_e(m) = \frac{|S_{ref}(m)|^2}{|S_{inc}|^2} \text{Re} \left[ \frac{k_{z,m}^{ref}}{k_z^{inc}} \right] \quad (3.138)$$

These equations hold if the values are calculated from electric fields. If magnetic field quantities were used then the equations would be

$$T_h(m) = \frac{|S_{trn}(m)|^2}{|S_{inc}|^2} \text{Re} \left[ \frac{k_{z,m}^{trn} \mathfrak{E}_{r,inc}}{k_z^{inc} \mathfrak{E}_{r,trn}} \right] \quad (3.139)$$

and

$$R_h(m) = \frac{|S_{ref}(m)|^2}{|S_{inc}|^2} \text{Re} \left[ \frac{k_{z,m}^{ref}}{k_z^{inc}} \right] \quad (3.140)$$

Once all of the diffracted modes are accounted for the over all reflectance and transmittance is given by adding up the individual quantities.

$$T_{tot} = \sum_M T(m) \quad (3.141)$$

$$R_{tot} = \sum_M R(m) \quad (3.142)$$

So far the model formulation has ignored loss, so that energy conservation should be 100%. To check for this one simply adds the transmittance and reflectance and you should get unity, which means 100%.

$$T_{tot} + R_{tot} = 1 \quad (3.143)$$

If the result is greater or less than 1 by a considerable amount, say 0.1, it is likely there is a problem with the model. If loss or gain were included it is best practice to initially run the model with these parameters ignored or “turned off” and check for conservation. Once lossless unity is verified, then it would safe to enable loss or gain and evaluate the model.

## Chapter 4: Results

The bulk of the literature on Dyakonov surface waves is on the theoretical analysis of DSW existence coupled with complex structures like LHM, photonic crystals and anisotropic materials. These papers investigate the dispersion these waves experience depending on the angle of the crystallographic axis, influence of cladding material, and the effect the combination of the two said parameters on the AED of DSWs. Aside from the publications using crystals some of these anisotropic materials have not been physically fabricated in a lab yet. This means that the published results are simulations or other analytics produced by advanced simulation software. The authors present dispersion curves and simulation results similar to what the 3D AFDFD and surface wave tools will produce. In the remainder of this chapter we will explore the dispersion of wave as influenced by the refractive index of the cladding, angle of allowed propagation due to the geometry symmetry of our materials, effect of birefringence on the AED and also duplicate a simulation from a published work.

We begin with a exploring the AED of device composed of an anisotropic crystalline structure and an isotropic cladding using the slab waveguide analysis of the previous chapter. The analysis is accomplished by first building the device onto a grid. Then you extract a vertical sliver of the grid to represent the slab waveguide based on the device parameters. The device itself would look similar to Figure 4.1

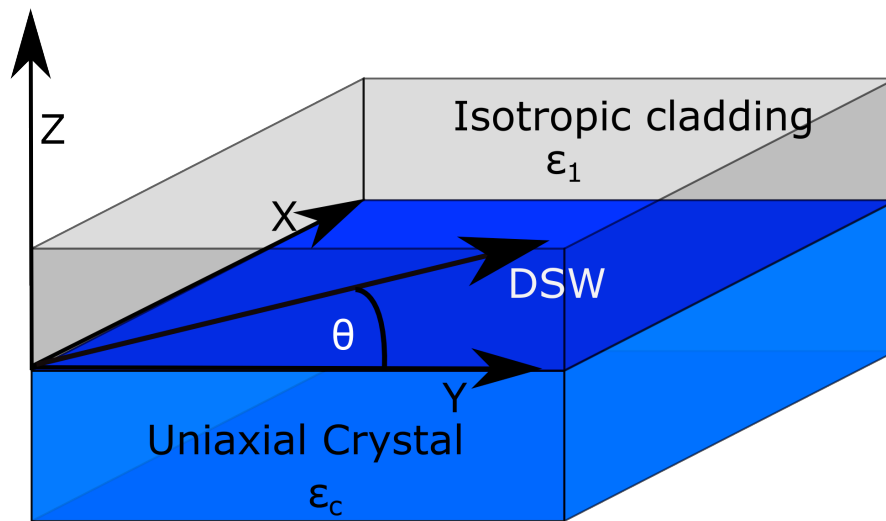


Figure 4.1 DSW basic configuration.

Where  $\epsilon_1$  permittivity of the cladding and  $\epsilon_c$  is permittivity tensor of the crystal. Using these permittivity values the surface wave tool can analytically evaluate the modes produced at the interface of the isotropic and anisotropic slabs when the conditions outlined in chapter 2 are satisfied. When characterizing the angle of propagation for the DSW, material parameters are rotated, in the tensor, to simulate physically turning the slabs as mentioned previously when drawing the device. In the below simulation the AED is defined from 30.2 to 37.4 degrees centered at approximately 34 degrees.

The surface wave analysis produces a combination of four wave components that are displayed in Figure 4.2. This graph shows you the results of the solving the set of four linear equations in chapter 3, however here each mode amplitude is scaled down to a quarter of its original size in order to be displayed clearly. The true amplitudes are shown in Figure 4.3. Each peak is result of one equation in the Eigenvalue problem. The first peak would be the profile of to the  $a_x$  component. The second describes the  $a_y$  component and so on, as you descend along the elements of the matrix  $[x]$  in equation (3.108). Of course, if a different grid layout was used these labels would change with respect to the variables in  $[x]$ .

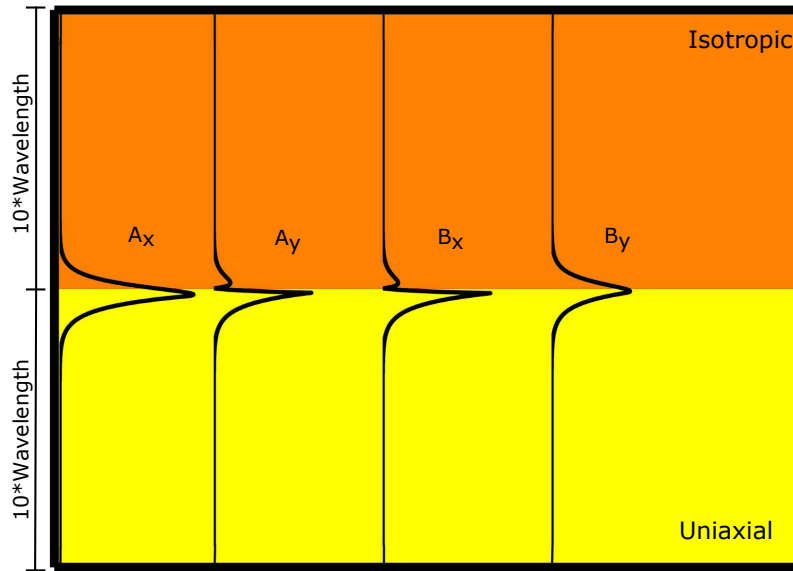


Figure 4.2 Example of surface modes.



Viewing the results in this way is not very intuitive as to what is actually going on in the device. Figure 4.2 actually shows a DSW at the center of AED and this is the case where the energy is best confined at the interface. To help visualize this the four components can be superimposed on each other and the device in a more valid representation of a real life scenario. The result of this would look something similar to Figure 4.3.

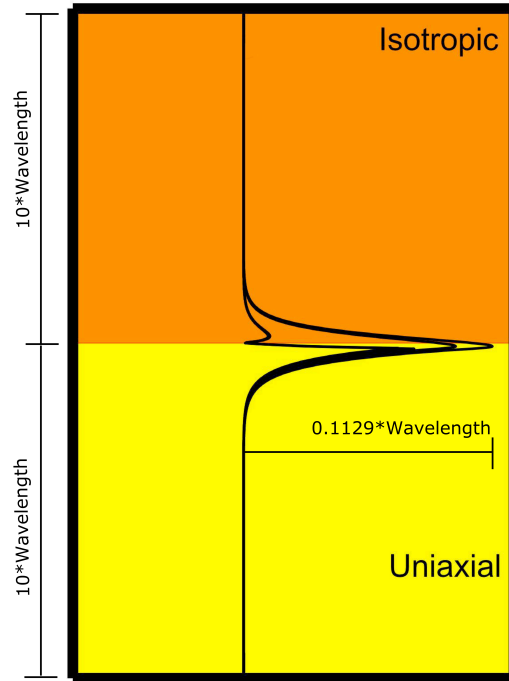


Figure 4.3 DSW Centered of AED.

In this orientation one can see how well confined the waves are as they propagate, when completely centered in the AED. This overlay orientation helps visualize the DSW's profile as its propagation changes from non-existence towards the minimum angle of the AED, then towards the center, followed by the max and finally as it decouples out and possibly transitions to a mode in the crystal slab. As the DSW travels to either end of the AED the energy tends to lean/or stretch to the left or right for the minimum and maximum of the AED respectively. To help illustrate this we simulate a DSW at the max of its AED. Figure 4.4 is the result of this simulation.

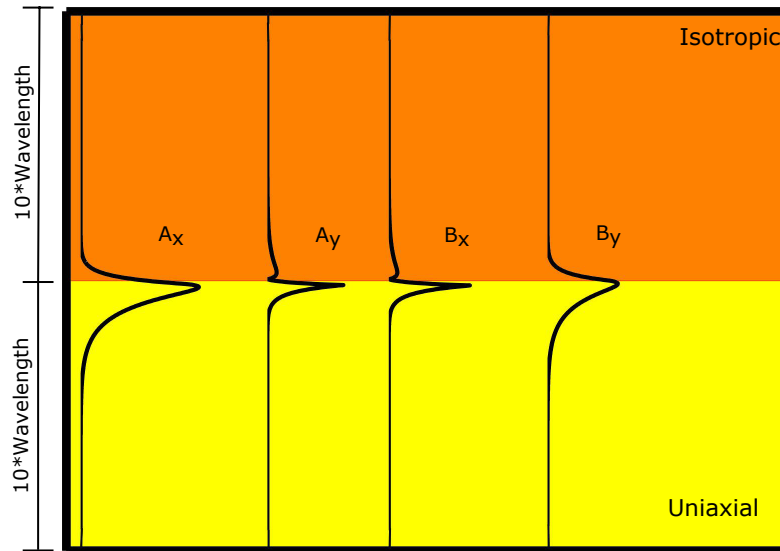


Figure 4.4 DSW Off Center of AED.

Again for a better visual of what is actually happen the four components are super imposed onto each other and back onto the device in Figure 4.5.

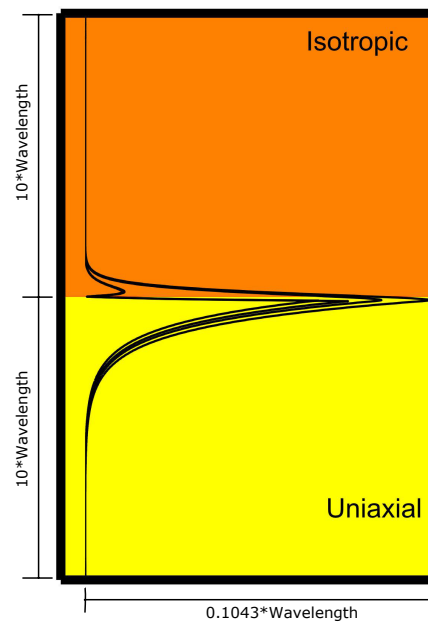


Figure 4.5 DSW Near Max of AED.

You will notice that the area under the decaying portion of the mode amplitudes increases as the energy stretches further away from the interface and into the uniaxial material as you span the AED. This is more apparent if you can view the images side by side like in Figure 4.6.

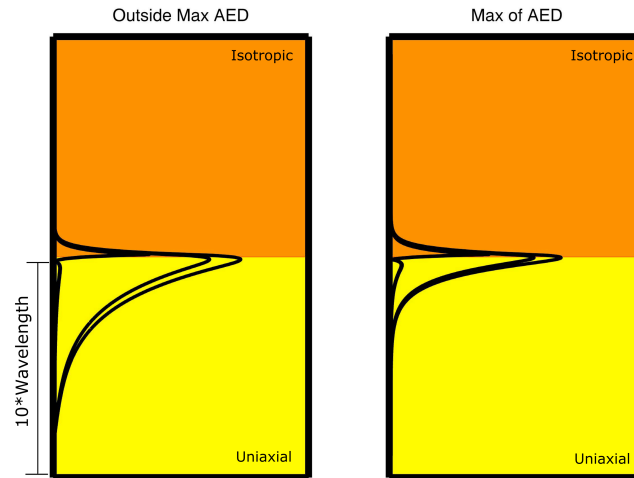


Figure 4.6 DSW transition out of AED.

The above figure clearly illustrates the energy changing from a more confined profile around the interface to beginning its transition into the anisotropic crystal in the lower half of the image. This is characteristic of the DSW operating at or around the maximum allowed angle in the AED, above this threshold the wave transfers energy in to the crystal and what happens after that can vary. At the case of the minimum angle the energy profile would be flipped and lean more towards the upper isotropic cladding.

The same tool could be used to observe the effects of altering the physical dimensions of the device being studied. All previous simulations describe two slabs of semi-infinite extent in both directions. In a physical mock of these devices that may not be possible so it would be advantageous to analyze the effects of limiting the dimensions of the device have on the DSW itself. Figure 4.7 illustrates one such simulation where height of the isotropic superstrate is reduced to the size of one wavelength. In this scenario it is clear that the dimensions influence the containment of the fields at the interface but the DSW is still excited under these reduce dimensions. The same is true for the other case where the uniaxial crystal is the dimension being reduced.

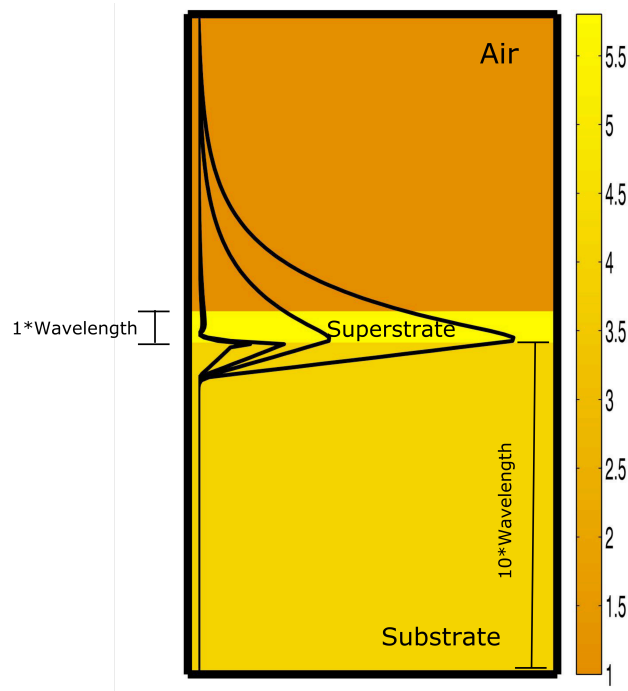


Figure 4.7 Physical limitation study

Because we can overlay simulated results onto our materials, as shown above, we can study the angular existence domain in ways the laboratory experiment cannot. Now, the angular existence domain created by our fictitious crystal is much larger than typical crystals because of its very large birefringence. Though the crystal does not currently exist, the characteristic properties of it are a byproduct of the analysis formulated previously. This analysis is only the first step in realizing future materials. It provides the freedom to imagine and test theoretical materials before proceeding to engineer them. In Ref. [3] the authors did the same by proving the possible existence of DSW resonance in photonic crystals using a material geometry that could be engineered to have the desired properties. Photonic crystals are unique in that they are a man made material, which can exhibit different properties depending at which limit of the wavelength the cell operates. Realizing this and using a unit cell at the long wavelength limit the photonic crystal produce enormous positive birefringence in the device. Other researchers used what are referred to as left-handed materials, to create a large AED, due to the device's large birefringence [13]. These are also artificially produced.

The positive uniaxial crystal developed above was characterized by  $n_x = 1.0925$ ,  $n_y = 1.0925$ , and  $n_z = 2.9$ . With the crystal properties known, the next step must be to find a value for the refractive

index of cladding that when mated to the crystal will satisfy equation (1.1). Due to the large index contrast between 2.9 and 1.0925 there are many possibilities of  $n_c$  that satisfy this stipulation. As numerous as the possibilities maybe they are bounded by the stipulations imposed equation (1.1) for a positive uniaxial crystal. This range of values is illustrated in Figure 4.8.

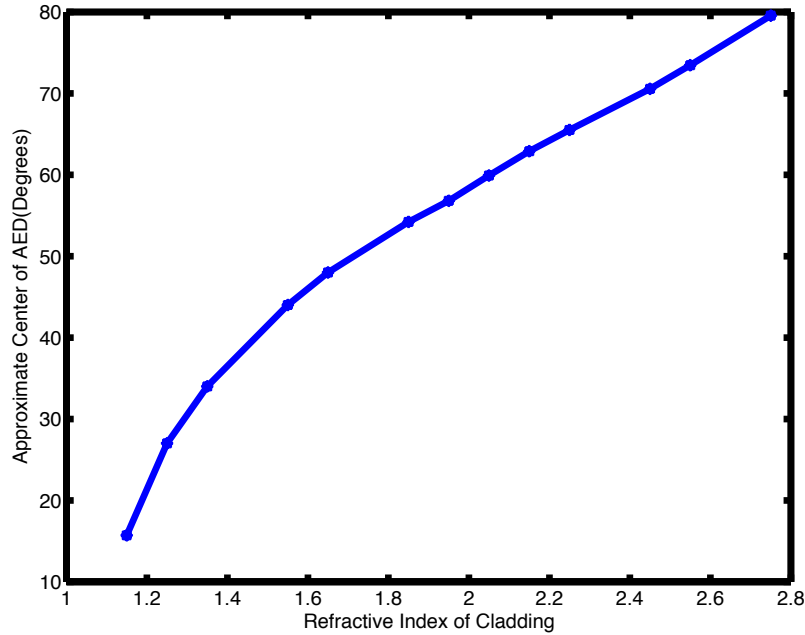


Figure 4.8 Effect of cladding on center point of the AED.

The figure above illustrates how as the refractive index of the cladding shifts so does the AED in an almost a linear fashion. This type of curve is very similar to the one presented by Takayama, Crasovan, Artigas and Torner, in [7]. Their study however was focused around the maximum point of the AED due the physical limitations of the experimental setup. Their experiment, seen in Figure 4.13, uses a technique, known as polarization conversion, which captures energy coupled to the these hybrid waves as a sharp increase of intensity across the reflection spectrum instead of a sharp dip [24]. It is this polarization conversion that allowed them to produce the results seen in Figure 4.9

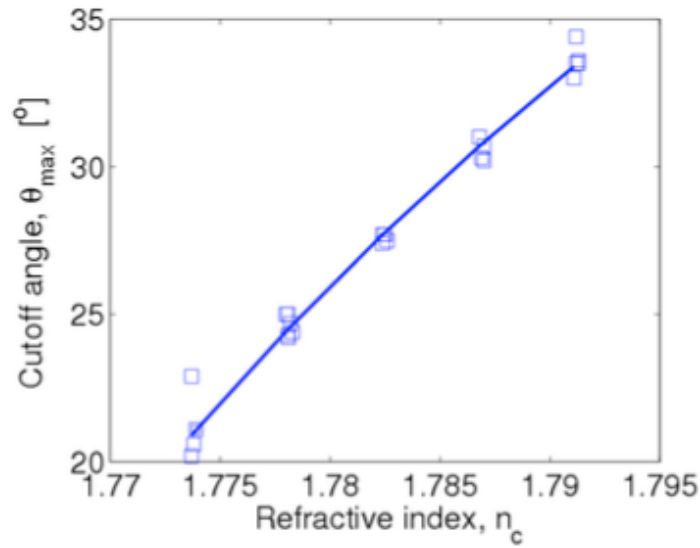


Figure 4.9 DSW AED Max Cut Off[7].

Both graphs show a similar behavior and illustrate the directionality these surface waves exhibit based on their isotropic cladding. This cladding, if it were an electro-optic material, could be adjusted in real time using the Pockel's effect to change the direction of these hybrid waves. This also indicates how these waves could be used in sensing applications as in influx of external agents into the vicinity of the device would cause a noticeable change in the DSW behavior due to their influence on the isotropic material at the boundary. It should be noted that while the Figure 4.8 describes the behavior around the central angle Figure 4.9 depicts the behavior of the wave at its maximum allowed angle.

There is second consequence to having a large birefringence in that there exists a “sweet spot”, so to say, in the value for the cladding that gives the largest possible AED. This optimal value of the isotropic cladding is said to be closer to the ordinary refractive index of the crystal as opposed to the extraordinary [1]. Using a hypothetical crystal, characterized by  $n_0 = 1.0925$  and  $n_e = 2.9$ , Figure 4.10 demonstrates where its optimal refractive index for the partnering cladding would be located. Here the optimum value for the cladding exists between  $n_c = 1.3$  and  $n_c = 1.5$  which is closer to the ordinary refractive index  $n_0$  than to extraordinary index  $n_e$ .

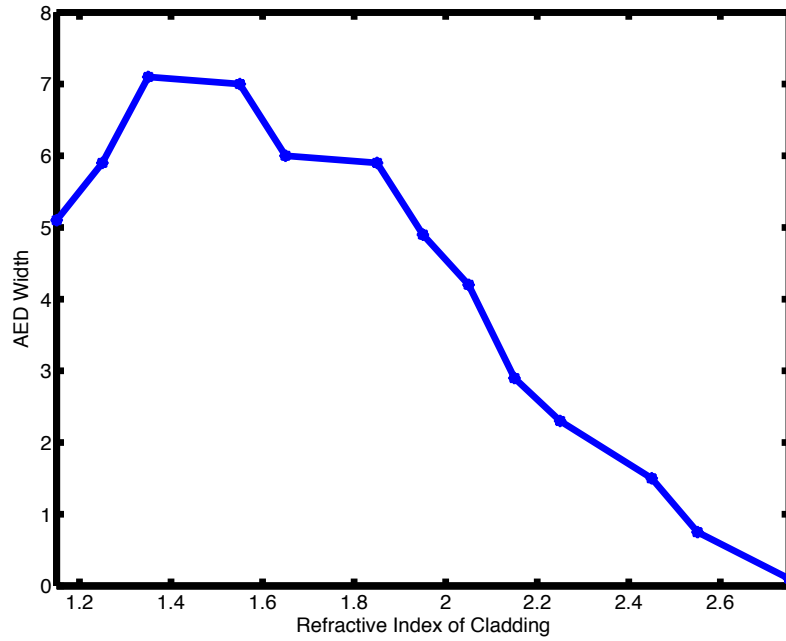


Figure 4.10 Width of AED

These results are based on a material with extremely large birefringence, which a characteristic not found in natural materials. With previously derived methodology, one can observe the effect the degree birefringence has on the AED when coupled with different values for the isotropic cladding. This is just a quicker way of analyzing the effect the birefringence of the crystal and refractive index of the cladding have on the angular existence domain as illustrated in Figure 4.11. The steep rise indicated in the graph showcases that at the AED would increase tremendously as you increase the degree of birefringence in the anisotropic material while centered at the optimal refractive index of the cladding. As you move away from the peak points the AED drops off to smaller domains indicated by the flat portions of the graph. These flat areas do not mean there are no DSWs supported there. These areas simply mean that the size the AED is much smaller than at the optimal point.

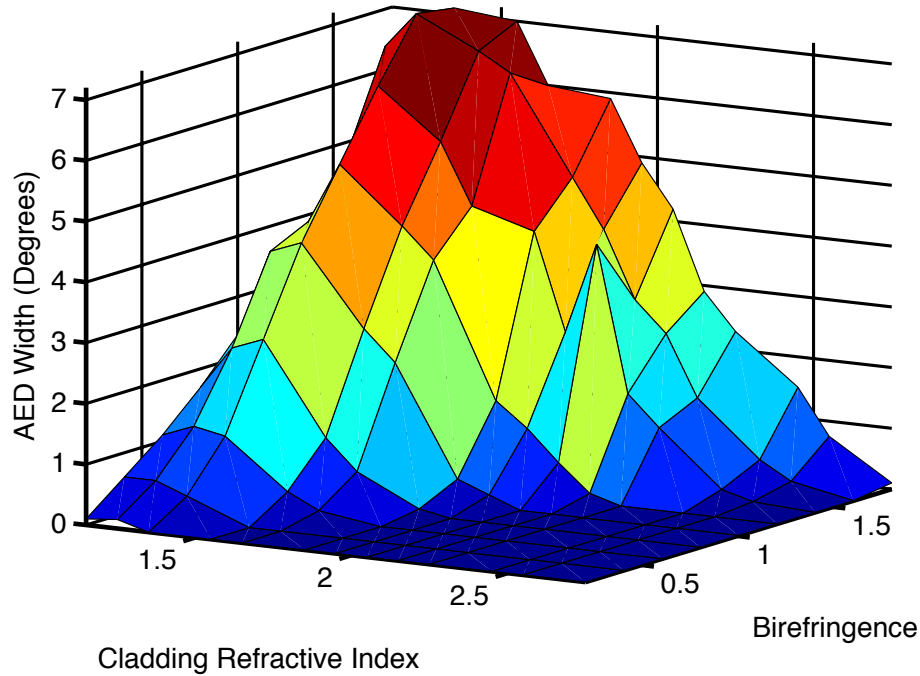


Figure 4.11 Effect of the birefringence and cladding on the AED.

This simulation sums up the most of the characteristics the surface wave analysis tool can analyze into one graph.

Before we proceed to the next section it is important to point out all over the above data could physically excited if the source used was a “pure” source. In most physical experiments the source used to excite a device is actually composed of a band of frequencies. This means that the device under study could be excited in multiple instances with each instance corresponding to one of the separate frequencies composing the incident beam. In a standard waveguide each one of these frequencies would experience a different phase accumulation resulting is some traveling faster than others and is depicted by the increasing (blue) line in Figure 4.12. This dispersion in the propagating energy and means that portions of that energy will arrive at different points in time at the end of the guide. This is very troublesome for as this has to accounted and correct for. In the case of DSW the response would be very linear and is seen in Figure 4.12 as the (red) flat line.



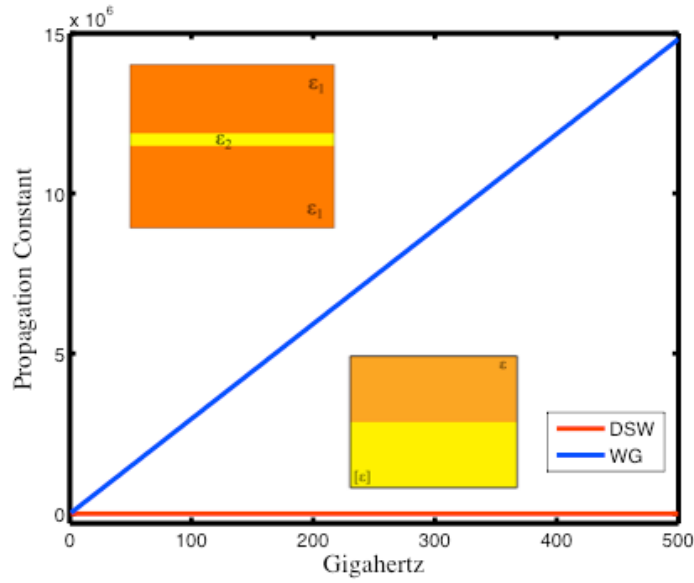


Figure 4.12 Frequency effect on the propagation constant.

While some have claimed that these hybrid waves at the interface can be analyzed very similar to waveguides this type of response is not typical normal waveguides. Normal waveguides can only guide discrete modes, at certain frequencies while the surface waves seem to be much more flexible.

So far the surface wave analysis has analyzed the possible modes that could exist at the interface of two materials. The next section will use the AFDFD to look at the actual excitation of Dyakonov surface waves using materials that currently exist and compare them to other published studies. The materials used in the literature to excite these types of waves are potassium titanyl phosphate (KTP) and lithium triborate (LBO), which are types of optically anisotropic crystals. Using an yttrium vanadate ( $\text{YVO}_4$ ) crystal used to predict excitation, we see just how difficult it is to actually perceive these elusive surface waves. The analysis of the  $\text{YVO}_4$  crystal is seen later in Figure 4.15

#### 4.1.1 Dyakonov Excitation

There are very few instances of actual DSW excitation in the 20 years since their discovery. One instance is seen in a paper published by Luis Torner [24] in which he illustrates the excitation of these hybrid phenomena using a modified Otto-Kretschman configuration and a technique known as polarization conversion spectroscopy. It is the combination of this technique and the experimental setup in Figure 4.13 that allowed for the very first recorded DSW excitation [7].

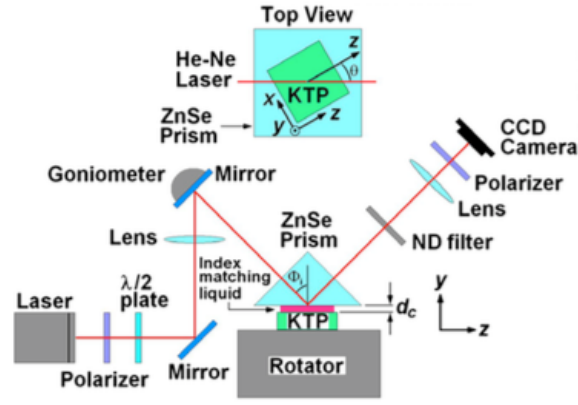


Figure 4.13 DSW Experimental Configuration[7].

While this would be a very complicated and tedious experiment to recreate, Torner uses a process where DSW excitation is initially predicted by simpler model of material analysis to predict if the materials support these hybrid waves. From there, these results are used to predict surface wave excitation in the full model. It is with the same methodology that the two algorithms presented in this work are utilized. We would start with the simpler surface wave model to verify if surface modes would exist in the materials. Then the AFDFD would explore their excitation with the more complex model. This sequential break down of the experiment would save time and effort, as problems in the models could be isolated faster than trying to resolve them straight from the complete model. One of the analytical models that will under go this sequential process is displayed in Figure 4.14.

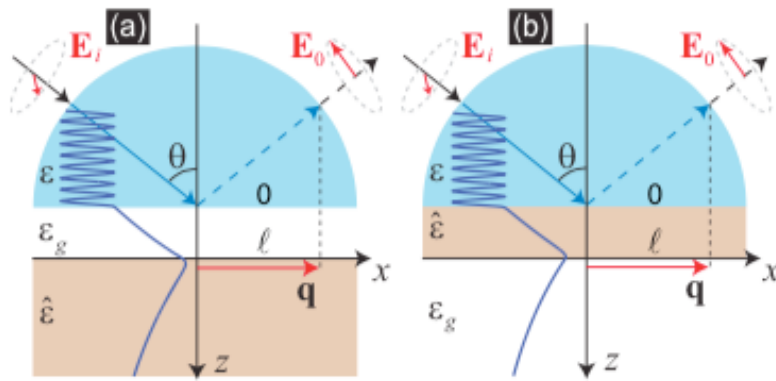


Figure 4.14 Torner DSW Analytical Configurations[24].

Torner uses these two configurations in various configurations with different materials to provide different images. One such image shows the characteristics these waves produce while on resonance and away from resonance.

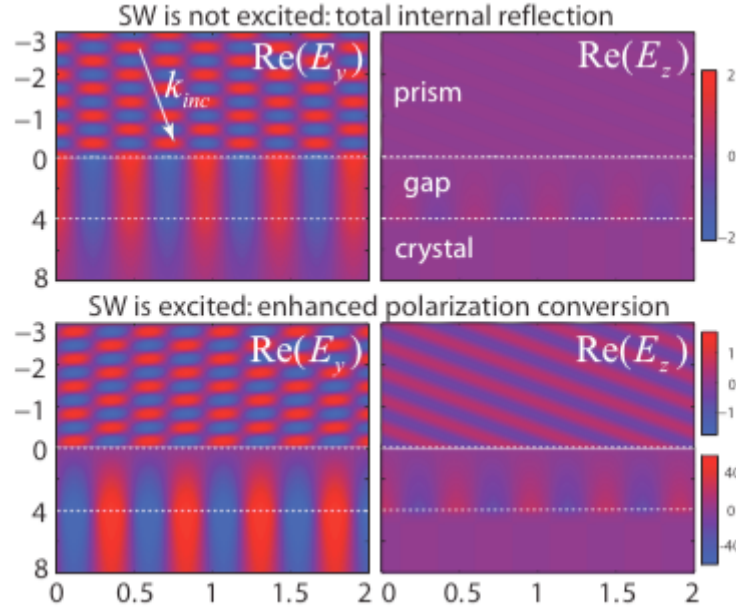


Figure 4.15 DSW Torner Simulation[24].

The parameters used above are would serve a good basis to test the AFDFD method presented prior. Using the same material parameters and thickness for each material in Figure 4.14a, the AFDFD model results in Figure 4.16.

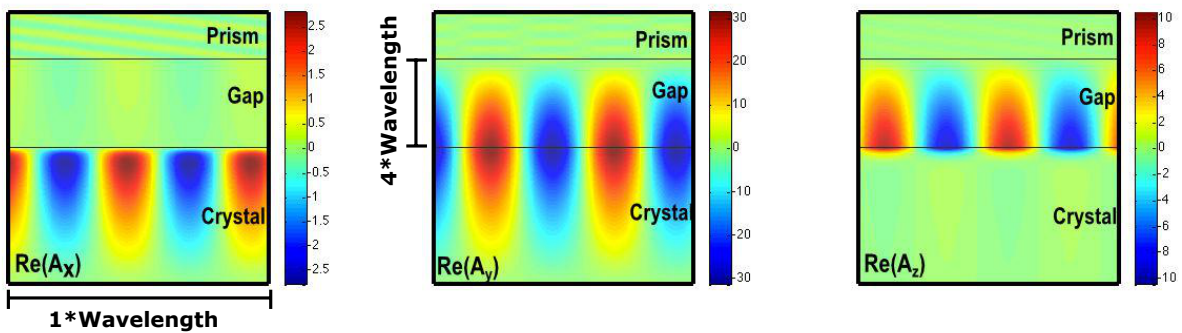


Figure 4.16 Polar Spectroscopy Verification.

The tool presents the amplitudes of all three field components for either the Electric or Magnetic field depending on which wave equation (3.114) or (3.115) is being evaluated. These three field images are very similar to what Toner presents Figure 4.15. He only showed the  $E_y$  and  $E_z$  components but

regardless of which grouping you choose to observe you see that there is energy confined to the interface of the two slabs as marked by the black line in Figure 4.16 or the dotted line in Figure 4.15.

## **Chapter 5: Conclusion**

Starting with Maxwell's equations, we have derived and formulated the means to rigorously model fully anisotropic electromagnetic materials in a package that can be outfitted for any coding language. While the results presented are producing using MATLAB the methodology presents all the required information that any one could then translate to any coding environment such as C or Python. This work is expected to expand the pool of resources available to simulate future applications of electromagnetics using anisotropic materials and it also provides the means to help design artificial material properties. After that it is up to the user to proceed with some material engineering combined with geometric manipulation of the crystal lattice to produce the final product.

## References

- [1] O. Takayama, L.-C. Crasovan, S. K. Johansen, D. Mihalache, D. Artigas, and L. Torner, “Dyakonov Surface Waves: A Review,” *Electromagnetics*, vol. 28, no. July 2007, pp. 126–145, 2008.
- [2] J. Polo, T. Mackay, and A. Lakhtakia, *Electromagnetic Surface Waves: A Modern Perspective*. Newnes, 2013.
- [3] D. Artigas and L. Torner, “Dyakonov surface waves in photonic metamaterials,” *Phys. Rev. Lett.*, vol. 94, no. January, pp. 1–4, 2005.
- [4] S. Chen, Z. Shen, and W. Wu, “Analysis of Dyakonov surface waves existing at the interface of an isotropic medium and a conductor-backed uniaxial slab,” *J. Opt. Soc. Am. A. Opt. Image Sci. Vis.*, vol. 31, no. 9, pp. 1923–30, Sep. 2014.
- [5] Z. Jacob and E. E. Narimanov, “Optical hyperspace for plasmons: Dyakonov states in metamaterials,” *Conf. Proc. - Lasers Electro-Optics Soc. Annu. Meet.*, pp. 563–564, 2009.
- [6] O. Takayama, D. Artigas, and L. Torner, “Practical dyakonons,” *Opt. Lett.*, vol. 37, no. 20, p. 4311, 2012.
- [7] O. Takayama, L. Crasovan, D. Artigas, and L. Torner, “Observation of dyakonov surface waves,” *Phys. Rev. Lett.*, vol. 102, no. January, pp. 2–5, 2009.
- [8] O. Takayama, A. Y. Nikitin, L. Martin-Moreno, L. Torner, and D. Artigas, “Dyakonov surface wave resonant transmission,” *Opt. Express*, vol. 19, no. 7, pp. 6339–6347, 2011.
- [9] O. Takayama, D. Artigas, and L. Torner, “Lossless directional guiding of light in dielectric nanosheets using Dyakonov surface waves,” *Nat. Nanotechnol.*, vol. 9, no. 2, pp. 419–24, 2014.
- [10] J. J. Miret, “Substantial enlargement of angular existence range for Dyakonov-like surface waves at semi-infinite metal-dielectric superlattice,” *J. Nanophotonics*, vol. 6, p. 063525, 2012.
- [11] J. a. Polo, S. Nelatury, and A. Lakhtakia, “Surface Electromagnetic Wave at a Tilted Uniaxial Bicrystalline Interface,” *Electromagnetics*, vol. 26, no. January 2012, pp. 629–642, 2006.
- [12] J. A. Polo, S. R. Nelatury, and A. Lakhtakia, “Surface waves at a biaxial bicrystalline interface,” *J. Opt. Soc. Am. A*, vol. 24, no. 9, pp. 2974–2979, 2007.
- [13] C. J. Zapata-Rodriguez, J. A. Sorni, S. Vukovic, L. E. Martinez, M. T. M. T. Caballero, J. J. Miret, C. J. Zapata-rodríguez, J. A. Sorní, S. Vukovi, L. E. Martínez, M. T. M. T. Caballero, and J. J. Miret, “Novel prospects in hyperbolic metamaterials: Dyakonov-like surface waves,” in *2014 16th International Conference on Transparent Optical Networks (ICTON)*, 2014, vol. 2, pp. 1–4.
- [14] K. Agarwal, J. a. Polo, and A. Lakhtakia, “Theory of Dyakonov-Tamm waves at the planar interface of a sculptured nematic thin film and an isotropic dielectric material,” pp. 1–12, 2009.

- [15] S. V. Pasechnik, V. G. Chigrinov, and D. V. Shmeliova, *Liquid Crystals: Viscous and Elastic Properties in Theory and Applications*. John Wiley & Sons, 2009.
- [16] A. Nelatury, S.R., Polo, J.A., Lakhtakia, "On Widening the Angular Existence Domain for Dyakonov Surface Waves using the Pockels Effect," *Microw. Opt. Technol. Lett.*, vol. 50, no. 9, pp. 895–896, 2008.
- [17] S. R. Nelatury, J. a. Polo, Jr., and a. Lakhtakia, "Electrical control of surface-wave propagation at the planar interface of a linear electro-optic materials and an isotropic dielectric material," no. September 2014, p. 14, 2007.
- [18] L. Torner, J. P. Torres, C. Ojeda, and D. Mihalache, "Hybrid waves guided by ultrathin films," *J. Light. Technol.*, vol. 13, no. 10, pp. 2027–2033, 1995.
- [19] R. C. Rumpf, "SIMPLE IMPLEMENTATION OF ARBITRARILY SHAPED TOTAL-FIELD/SCATTERED-FIELD REGIONS IN FINITE-DIFFERENCE FREQUENCY-DOMAIN," *Prog. Electromagn. Res. B*, vol. 36, pp. 221–248, 2012.
- [20] K. S. Yee, "Numerical Solution of Initial Boundary Value Problems Involving Maxwell's Equations in Isotropic Media," *Antennas Propag.*, vol. 14, no. 3, pp. 302 – 307, 1966.
- [21] R. C. Rumpf, C. R. Garcia, E. A. Berry, and J. H. Barton, "Finite-difference Frequency-domain Algorithm for Modeling Electromagnetic Scattering from General Anisotropic Objects," vol. x, no. July, 2014.
- [22] R. C. Rumpf, "Implementation of Finite-Difference Frequency-Domain." [Online]. Available: <http://emlab.utep.edu/ee5390cem/Lecture 13 -- FDFD Implementation.pdf>. [Accessed: 13-Apr-2015].
- [23] R. C. Rumpf, A. Tal, and S. M. Kuebler, "Rigorous electromagnetic analysis of volumetrically complex media using the slice absorption method.," *J. Opt. Soc. Am. A. Opt. Image Sci. Vis.*, vol. 24, no. 10, pp. 3123–3134, 2007.
- [24] a Y. Nikitin, D. Artigas, L. Torner, F. J. García-Vidal, and L. Martín-Moreno, "Polarization conversion spectroscopy of hybrid modes.," *Opt. Lett.*, vol. 34, pp. 3911–3913, 2009.

## **Vita**

Jose Luis Enriquez Jr, was born in El Paso, Texas to Maria and Jose Luis Enriquez Sr. and is the oldest of their three sons. He graduated from J. M. Hanks High School in 2003 and enrolled into the University of Texas at El Paso later that year. In 2008 he was awarded his B.S. in Electrical and Computer Engineering and took a job for the nuclear section of US Army out at White Sands Missile Range. After 5 years on the job he decided to return to the University of Texas at El Paso in search of a master's degree. After a year and a half of classes he join the up and coming EMLab headed by Dr. Raymond Rumpf.

Permanent address: 1713 Tommy Aaron  
El Paso, Texas 79936

This thesis/dissertation was typed by Jose L. Enriquez Jr.